https://doi.org/10.5194/egusphere-2026-6522
Preprint. Discussion started: 19 November 2026
© Author(s) 2026. CC BY 4.0 License.

Monitoring Fracture Evolution and Calving Precursors on Totten Ice Shelf Using ICESat-2

Cheng Cheng and Ian Willis

Scott Polar Research Institute, University of Cambridge, Lensfield Road, Cambridge CB2 1ER, UK

Correspondence: Cheng Cheng (gaussc2014@gmail.com)

Abstract. Totten Glacier is a major contributor to mass loss from East Antarctica, and the stability of its floating ice shelf is strongly influenced by fracture development and iceberg calving. However, the vertical structure and temporal evolution of ice shelf fractures remain poorly constrained by conventional satellite imagery. Here, we present the first systematic analysis of fracture distribution, evolution, and calving dynamics on Totten Ice Shelf using ICESat-2 ATL06 data acquired between 2018 and 2025. A novel normalised cross-correlation (NCC)-based matching algorithm was developed and used together with a hierarchical fracture-detection algorithm to extract fracture characteristics and track individual fractures through successive ICESat-2 observations. We use the depth-to-freeboard ratio (D/F), defined as fracture depth relative to the local ice-shelf freeboard, as a measure of fracture penetration and structural damage. Calving precursor fractures exhibit higher D/F values than non-precursor fractures, with D/F providing stronger discrimination of calving fractures than the depth-to-width ratio (D/W). Spatially, the highest D/F values occur in frontal regions connected to basal channels, while the inter-channel region between two major channels exhibits consistently low fracture development, potentially reflecting suture zone-like material heterogeneity. Analysis of fracture time series and annual D/F distributions reveals a consistent pre-calving sequence in which fracture penetration first reaches sea level near basal-channel boundaries before extending across the full fracture length. Major calving events occur shortly after D/F values become continuous along the frontal fracture system. These observations provide a basis for a proposed short-term calving-monitoring framework based on the spatial and temporal evolution of D/F. The NCC-based matching method further enables automated tracking of individual fractures across repeat ICESat-2 observations and provides a transferable approach for monitoring fracture evolution on Antarctic ice shelves.

1. Introduction

Ice shelves play a key role in regulating the discharge of grounded ice from Antarctica by providing buttressing to upstream ice flow (Dupont & Alley, 2005). Changes in ice-shelf thickness, flow, and structural integrity can therefore influence the stability of the grounded ice sheet and its contribution to sea-level rise. Totten Glacier is one of the largest contributors to mass loss in East Antarctica, with an average ice discharge of 83 ± 0.3 Gt yr^{-1} since 2016 (Davison et al., 2025). It drains the Aurora Subglacial Basin, where much of the bed lies below sea

https://doi.org/10.5194/egusphere-2026-6522
Preprint. Discussion started: 19 November 2026
© Author(s) 2026. CC BY 4.0 License.

level, making the basin potentially vulnerable to marine ice sheet instability (Aitken et al., 2014). The ice volume contained within the Totten drainage system corresponds to at least 3.5 m of global mean sea-level rise (Greenbaum et al., 2015), highlighting the importance of understanding the processes that regulate the stability of Totten Glacier and its floating ice shelf.

Iceberg calving is a major component of ice shelf mass loss, and Totten Ice Shelf has one of the highest calving rates among East Antarctic ice shelves (Depoorter et al., 2013; Rignot et al., 2013; Qi et al., 2021). Calving is closely associated with fracture development, as fractures can progressively weaken an ice shelf and, when sufficiently deep or interconnected, facilitate the detachment of large icebergs. Classical calving theories have emphasised the importance of fractures penetrating through the full ice thickness to sea level (Benn et al., 2007), while more recent work has highlighted multiple calving regimes and transitions between them as important controls on large and difficult-to-predict calving events (Alley et al., 2023). Despite these advances, the evolution of individual fractures from initial damage to full-thickness penetration, and its relationship to major calving events, remain poorly constrained observationally.

Satellite remote sensing has enabled the distribution and evolution of ice shelf fractures to be monitored over large spatial and temporal scales. Optical imagery from Landsat and Sentinel-2 and synthetic aperture radar (SAR) imagery from Sentinel-1 have been widely used to map fracture networks across Antarctic ice shelves (Wesche et al., 2013), while recent deep-learning approaches have enabled automated extraction of surface fractures over large areas (Pang et al., 2023). These approaches primarily characterise the two-dimensional surface expression of fractures, however, and therefore provide limited information on their vertical development. This limitation is important because the degree to which a fracture penetrates the ice thickness provides a physically meaningful measure of structural damage and is closely related to calving potential (Benn et al., 2007). Observations that can constrain fracture depth and its evolution through time are therefore needed to investigate how fracture damage develops toward calving.

The launch of the Ice, Cloud, and land Elevation Satellite-2 (ICESat-2) in September 2018 provided a new opportunity to characterise fracture geometry from repeated laser-altimetry observations (Markus et al., 2017). ICESat-2 provides high-resolution along-track measurements of surface elevation, allowing the topographic signatures associated with fractures to be resolved and tracked through time. Several recent studies have demonstrated the potential of ICESat-2 laser altimetry data for fracture or rift monitoring on Antarctic ice shelves. Walker and Gardner (2019) demonstrated the potential of ICESat-2, together with earlier ICESat observations, for characterising the surface topography and evolution of rifts across Antarctic ice shelves. Wang et al. (2021) subsequently developed a hierarchical fracture-detection algorithm for ICESat-2 ATL06 data and demonstrated its ability to extract fracture characteristics including depth and morphology. Building on this approach, Wang et al. (2025) introduced the depth-to-freeboard ratio (D/F), defined as the observed fracture depth relative to the theoretical depth required for the fracture to reach sea level, as a quantitative measure of fracture damage and showed for Thwaites Ice Shelf that larger D/F values were associated with more advanced structural damage and greater calving potential.

https://doi.org/10.5194/egusphere-2026-6522
Preprint. Discussion started: 19 November 2026
© Author(s) 2026. CC BY 4.0 License.

Despite these advances, the temporal evolution of fracture damage on Totten Ice Shelf remains poorly constrained. Totten Ice Shelf also contains a dense network of transverse and longitudinal fractures near its calving front, associated with its fast flow and frequent calving of large tabular icebergs (Cook et al., 2018; Wesche et al., 2013). Cook et al. (2018) investigated the mechanical controls on fracture and calving on Totten Ice Shelf using modelling approaches, providing important insight into the processes that may govern calving. However, direct observations of how fracture geometry and structural damage evolve through time and culminate in major calving events are lacking. In particular, it remains unclear how fracture damage varies spatially across the ice shelf, how it relates to basal channel geometry, and whether consistent temporal patterns precede major calving events.

Here, we use ICESat-2 ATL06 observations from 2018 to 2025 to investigate the spatial distribution, vertical structure, and temporal evolution of fractures on Totten Ice Shelf. We develop a novel normalised cross-correlation (NCC)-based matching algorithm and together with a hierarchical fracture-detection framework we apply it to identify and track individual fractures across repeated ICESat-2 observations. We address three main questions. First, how are fracture characteristics and structural damage distributed across Totten Ice Shelf, and how are these patterns related to basal channels? Second, how does the inferred structural damage of individual fractures evolve through time as they develop toward calving? Third, do major calving events exhibit a consistent sequence of fracture development that can provide a basis for short-term calving prediction? By combining spatial analyses, multi-year fracture tracking, and detailed examination of major calving events, we develop an observational approach for quantifying fracture evolution and its relationship to calving on Totten Ice Shelf.

2. Study Area and Data

2.1 Study Area

The Totten Ice Shelf is in Wilkes Land, East Antarctica (Fig.1). It is a 6200 km² floating extension of Totten Glacier and forms one of the major outlets of the Aurora Subglacial Basin, where the glacier system is largely grounded below sea level and therefore vulnerable to marine ice sheet instability and ocean-driven perturbations (Aitken et al., 2014; Greenbaum et al., 2015). As the most dynamic drainage system in East Antarctica, Totten Glacier discharges more ice annually than any other regional glacier and holds a total sea-level rise equivalent of at least 3.5 m (Greenbaum et al., 2015). Spatially, the ice shelf exhibits a clear thickness gradient, extending ~ 150 km northward from the grounding line to the calving front. Its ice thickness reaches a maximum of over 2.5 km at the grounding line and thins down to nearly 200 m at the calving front (Gwyther et al., 2011).

Driven by the persistent intrusion of modified Circumpolar Deep Water (mCDW), the Totten Ice Shelf experiences intense ocean-driven bottom melting. For the 2007–2008 period, Totten exhibited an area-averaged basal melt rate of 10.5 ± 0.7 m yr^{-1} that was the highest among all East Antarctic ice shelves, corresponding to a total basal melt mass of 63.2 ± 4 Gt yr^{-1} (Rignot et al., 2013). This localized and intense ocean thermal forcing actively carves the underside of the ice, giving rise to distinct basal channels aligned with sub-ice-shelf ocean flow (Lilien et al., 2025). Furthermore, the Totten Ice Shelf shows a dense network of transverse and longitudinal fractures close to its calving front, which is characteristic of fast-flowing Antarctic ice shelves and is associated with frequent calving of tabular icebergs (Cook et al., 2018; Wesche et al., 2013). This intensive structural breakdown sustains a substantial calving flux, with an average calving rate of 35 Gt yr^{-1} between 2005 and 2020, ranking second

https://doi.org/10.5194/egusphere-2026-6522
Preprint. Discussion started: 19 November 2026
© Author(s) 2026. CC BY 4.0 License.

highest in East Antarctica (Qi et al., 2021). Together, the intense basal melt and the dense fracture network make the Totten Ice Shelf a critical site for examining the relationship between fracture evolution, basal channels and ice shelf calving processes.

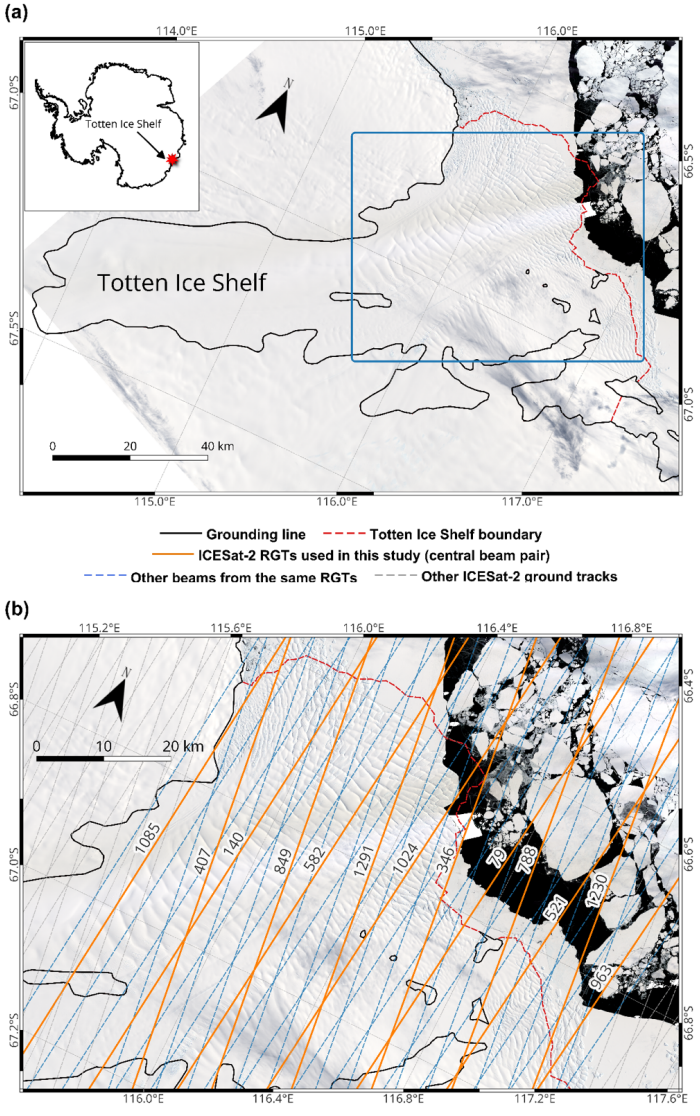


Figure 1. (a) Overview of the Totten Ice Shelf. The background imagery is a Landsat 8 image acquired on 29 November 2020. The solid black line shows the grounding line, while the dashed red line represents the Totten Ice Shelf boundary; both datasets are sourced from the MEaSUREs Antarctic Boundaries from Satellite Radar, Version 2 (Mouginot et al., 2017). The blue rectangle indicates the spatial extent of the zoomed-in area shown in (b). (b) Detailed view of the calving front and surface fractures with ICESat-2 ground tracks. The reference ground tracks (RGTs) used in this study are shown as orange solid lines and labelled by their RGT numbers (central beam

https://doi.org/10.5194/egusphere-2026-6522
Preprint. Discussion started: 19 November 2026
© Author(s) 2026. CC BY 4.0 License.

pair: gt2l & gt2r), the remaining beams from the same RGTs are displayed as blue dashed lines, and all other ICESat-2 ground tracks are shown as grey dashed lines.

2.2 ICESat-2 Data

ICESat-2 (Ice, Cloud, and Land Elevation Satellite-2) was launched on 15 September 2018 as the successor to the original ICESat mission (2003–2009). It carries the Advanced Topographic Laser Altimeter System (ATLAS), a photon-counting laser altimeter that operates at 532 nm (green) with a high pulse repetition rate of 10 kHz. This frequency achieves a fine along-track sampling interval of ~ 0.7 m on the Earth's surface (Markus et al., 2017). ATLAS emits six laser beams organized into three pairs; each pair consists of one strong and one weak beam to facilitate across-track slope determination and to compensate for the varying reflectivity of different surface types. These six ground tracks are designated GT1L, GT1R, GT2L, GT2R, GT3L, and GT3R based on their relative across-track positions (hereafter abbreviated as GTNX). In this nomenclature, "N" identifies the beam pair (1–3), and "X" denotes the left ("L") or right ("R") beam within each pair relative to the flight direction (Neumann et al., 2023). Within each pair, beams are separated by ~ 90 m, while adjacent pairs are spaced 3.3 km apart.

In this study, ATL06 Version 7 land-ice height data (Smith et al., 2025) acquired between 21 October 2018 and 8 December 2025 were used. All 13 ICESat-2 reference ground tracks (RGTs) that cross the Totten Ice Shelf and intersect the calving front were selected, and measurements from all six laser beams (both strong and weak beams) were analysed (Fig. 1b). Data coverage over the Totten Ice Shelf was first inspected using the OpenAltimetry platform (https://openaltimetry.earthdatacloud.nasa.gov). Acquisition dates with no data or only very limited spatial coverage were manually excluded. The remaining ATL06 data were subsequently downloaded via the National Snow and Ice Data Center (NSIDC, https://nsidc.org/data/atl06/versions/7). The dynamic atmospheric and ocean tide corrections were applied (Wang et al., 2021), and elevations were referenced to the EGM2008 Geoid.

2.3 Sentinel-1 Imagery

To validate the detected fractures and calving activities, Level-1 Ground Range Detected (GRD) products from the Sentinel-1A satellite were used, accessed via the Google Earth Engine (GEE) platform (Gorelick et al., 2017). These data additionally provided higher-resolution information on the spatial distribution of fractures and the temporal frequency of calving events, enabling more detailed interpretation of ice-shelf dynamics. SAR imagery was preferred over optical imagery due to its ability to provide consistent, all-weather, and year-round observations, unaffected by cloud cover or polar darkness. Specifically, data acquired in Extra Wide (EW) swath mode with HH polarization during the ascending orbit pass were selected, covering the period from October 2018 to April 2026. EW swath mode provides a 400 km swath width and a nominal spatial resolution of 20 × 40 m (Torres et al., 2012). This configuration is particularly well-suited for large-scale ice shelf monitoring. Only data from ascending orbits were used to maintain a consistent viewing geometry. This minimised variations in shadow orientation and geometric distortion between images, improving the reliability of fracture identifications and calving detection.

https://doi.org/10.5194/egusphere-2026-6522
Preprint. Discussion started: 19 November 2026
© Author(s) 2026. CC BY 4.0 License.

The Sentinel-1 imagery serves four primary purposes in this study. First, it is used to identify and characterize calving events at the Totten Ice Shelf front, providing estimates of their timing and spatial extent. Due to the repeat cycle of Sentinel-1 data, the exact timing of calving cannot always be determined. In such cases, the event date is estimated as the midpoint between the last image showing the complete fracture and the first image confirming the calving; the gap between these two dates represents the temporal uncertainty. Second, the Sentinel-1 imagery helps determine which fractures detected in ICESat-2 profiles eventually led to calving, providing an independent reference for the dataset described in Section 4.3. Third, it provides context to assist in matching fractures between repeat ICESat-2 passes, especially when the correlation-based matching is unclear, as described in Section 3.2. Finally, it is used to identify and remove false detections caused by drifting icebergs or other factors, thereby improving the overall quality of the auto-detected fracture dataset.

3. Methods

3.1 Fracture Detection and Characterisation

Ice shelf surface fractures were detected from ICESat-2 ATL06 data using the hierarchical, object-oriented approach developed by Wang et al. (2021). The analysis was applied to all 13 ICESat-2 reference ground tracks (RGTs) crossing the calving-front region of Totten Ice Shelf (66.6°–67.2°S). The detection procedure identifies fracture-like surface depressions in the one-dimensional along-track elevation profiles and characterises their geometric properties.

The fracture-detection algorithm uses a hierarchical bottom-up structure to identify local elevation minima and their associated pour points. A pour point is defined as the lowest elevation along the boundary of a depression, corresponding to the lower edge over which water would overflow. The pour level is the horizontal plane at the elevation of the pour point. For each depression, fracture depth (D) is calculated as the vertical elevation difference between the pour level and the bottom of the fracture (Fig. 2). To identify fractures over a range of spatial scales, adjacent depressions sharing a common pour point are iteratively merged to form higher-level depression features. The maximum hierarchical level was set to 20, compared to the maximum level of 10 used by Wang et al. (2021). This higher level was selected to account for the complex surface topography near the Totten Ice Shelf calving front, where mélange and numerous small surface crevasses can generate small-scale depressions that may obscure deeper and wider fracture features.

https://doi.org/10.5194/egusphere-2026-6522
Preprint. Discussion started: 19 November 2026
© Author(s) 2026. CC BY 4.0 License.

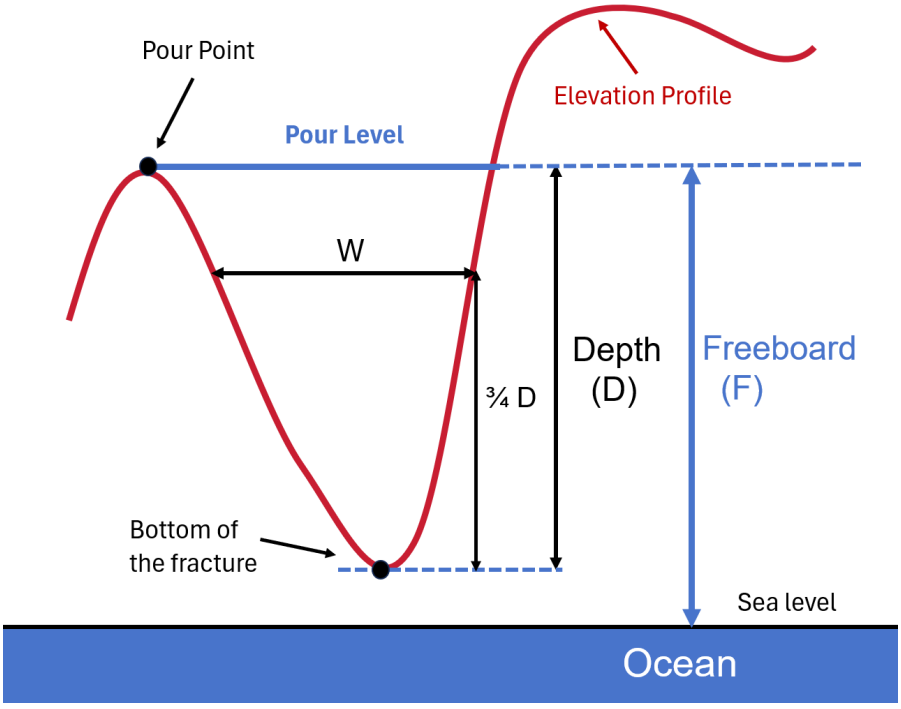


Figure 2. Diagram illustrating the key geometric parameters used to characterise a surface fracture detected from an ICESat-2 along-track elevation profile. The red solid curve represents the elevation profile. The blue solid line indicates the pour level. Fracture depth (D), Freeboard (F) and width at three-quarters depth (W) are all labelled in this diagram.

For each detected depression, several geometric characteristics were calculated (Fig. 2). The fracture width at three-quarter depth, W, is defined as the horizontal distance of the fracture at 75% of its total depth. This metric provides a more robust measure of fracture geometry than the full-width measurement, as it is less sensitive to surface slopes at the fracture edges. Freeboard (F) is the vertical distance from sea level to the pour level. Two ratios were subsequently calculated for each fracture: the depth-to-freeboard ratio (D/F) and the depth-to-width ratio (D/W). D/F, defined as the ratio of fracture depth to the local freeboard, therefore represents the fraction of the freeboard penetrated by the fracture. A value approaching 1 indicates that the fracture penetrates nearly to sea level, while D/F = 1 corresponds to a fracture depth equal to the local freeboard. Higher D/F values therefore indicate greater vertical penetration and, consequently, more advanced fracture damage (Wang et al., 2025). D/W, defined as the ratio of depth to width at three-quarters depth, characterises the aspect ratio of the fracture cross-section, with larger values indicating relatively deep and narrow fractures and smaller values indicating relatively wide and shallow fractures.

The detected depressions were subsequently filtered to retain features consistent with fracture morphology. Three morphological criteria were applied: a minimum D of 5 m, a maximum W of 3000 m, and a minimum D/W of

https://doi.org/10.5194/egusphere-2026-6522
Preprint. Discussion started: 19 November 2026
© Author(s) 2026. CC BY 4.0 License.

0.008. Because the hierarchical algorithm can identify the same physical feature at multiple levels, a parent-child selection procedure was then applied to reduce duplicate detections. Within the hierarchy, a parent depression is a higher-level feature containing one or more lower-level child depressions. Where both the child-to-parent depth ratio and the child-to-parent D/W exceeded 0.7, the child depression was retained, and the parent depression was discarded. These criteria were determined empirically through visual inspection of representative elevation profiles and comparison with the corresponding ATL06 measurements, with the aim of retaining physically plausible fractures while removing detections associated with background surface topography, mélange, and small-scale surface roughness.

The resulting fracture dataset contains the detected surface fractures and their associated geometric characteristics for each ICESat-2 track, including fracture location, depth (D), width (W), D/F and D/W. Examples of the detected fractures and their corresponding ICESat-2 elevation profiles are shown in Figure 3.

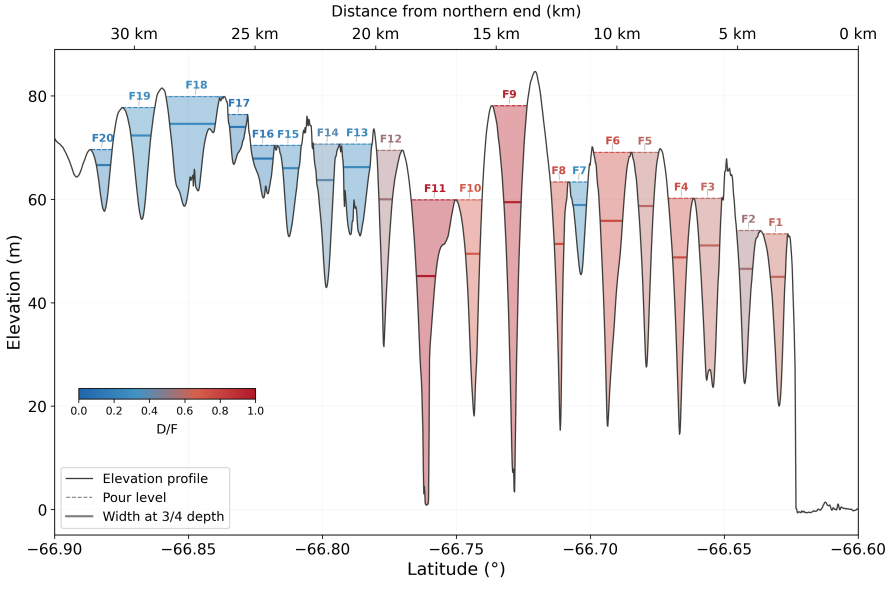


Figure 3. Example output of the fracture detection algorithm applied to the along-track elevation profile of ICESat-2 track 0582, beam gt2r, acquired on 4 November 2019 over Totten Ice Shelf. Detected fractures are highlighted by colour-filled regions between the pour level and the bottom of the fracture, with colours indicating the depth-to-freeboard ratio (D/F): red indicates high D/F, blue indicates low D/F, and grey indicates intermediate values. Fractures are labelled sequentially from F1 at the calving front end to the most inland detected fracture, based solely on detections from this beam and acquisition date.

3.2 Along-track Fracture Matching

To track individual fractures through time, a segment-based normalised cross-correlation (NCC) algorithm was developed to match fracture features between repeat ICESat-2 observations of the same RGT. The complete workflow is shown in Figure 4. NCC-based feature tracking has previously been applied to repeat satellite

https://doi.org/10.5194/egusphere-2026-6522
Preprint. Discussion started: 19 November 2026
© Author(s) 2026. CC BY 4.0 License.



altimetry profiles to measure ice-shelf surface displacement (Marsh & Rack, 2012; Breyer et al., 2020). Marsh & Rack (2012) demonstrated that correlations of large-scale surface undulations between repeat ICESat profiles could be used to estimate ice velocity on the Ross Ice Shelf, while Breyer et al. (2020) extended this approach to ICESat-2 data on the Foundation Ice Stream. Here, we adapt this concept to match individual fracture features between repeat ICESat-2 profiles and thereby quantify their spatial and geometric evolution through time.

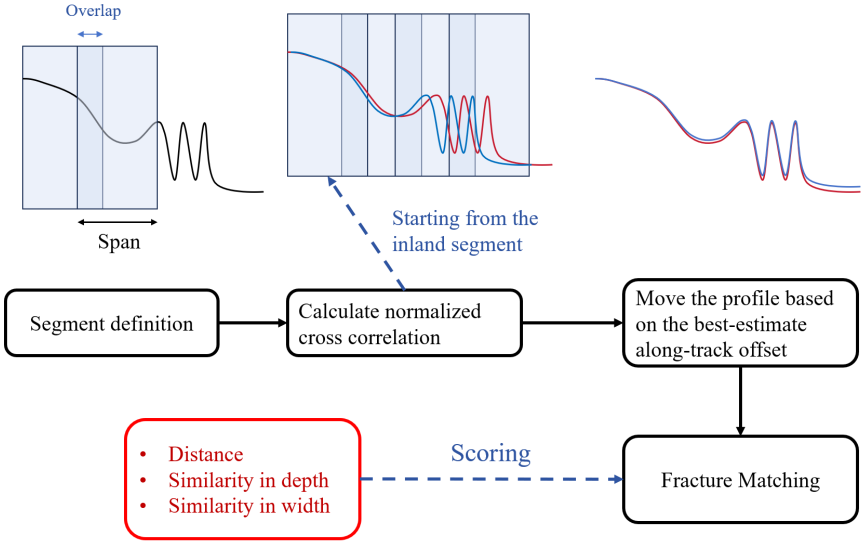


Figure 4. Workflow of the segment-based normalised cross-correlation (NCC) algorithm for fracture matching between successive ICESat-2 repeat tracks. Black boxes and connecting arrows indicate the main processing steps. Schematic along-track ICESat-2 elevation profiles are shown above the corresponding workflow boxes to illustrate the input data and intermediate outputs at each stage of the algorithm.

3.2.1 Segment Definition

Rather than correlating an entire along-track profile using a single displacement, each ICESat-2 profile was divided into a series of overlapping segments extending from the inland part of the study area towards the calving front. Each segment was 3 km in length, with an overlap of 1 km between adjacent segments and a resultant step size of 2 km. This segmentation accounts for the spatially variable ice velocity across Totten Ice Shelf, where along-track displacement generally increases towards the calving front. A single displacement applied to the entire profile would be unable to account for this velocity gradient. Independent NCC calculations were consequently performed for each segment, allowing the local along-track displacement to be determined and applied when matching fractures between repeat observations.

The segment length and overlap were determined empirically through iterative testing to provide sufficient spatial coverage for reliable correlation while retaining sensitivity to local displacement variations. To reduce edge effects and ensure that fractures located near segment boundaries were captured, an additional padding of 500 m was

https://doi.org/10.5194/egusphere-2026-6522
Preprint. Discussion started: 19 November 2026
© Author(s) 2026. CC BY 4.0 License.

added to each side of each segment. The padding was increased by 300 m for each additional repeat cycle, accounting for the accumulation of ice displacement between observations.

3.2.2 Normalised Cross-Correlation (NCC)

For each pair of repeat observations, the earlier observation was designated pass A and the later observation pass B. Within each segment, the ATL06 elevation values were centred by subtracting the mean elevation of the segment from each profile. This zero-mean transformation removes differences in absolute elevation between observations and ensures that the NCC primarily measures the similarity of the along-track elevation structure.

The along-track displacement between passes A and B was then estimated by calculating the normalised cross-correlation between the two elevation profiles:

$$\mathrm{NCC}(\tau) = \frac{\sum_x \widetilde{e_A}(x)\,\widetilde{e_B}(x+\tau)}{\sqrt{\sum_x \widetilde{e_A}(x)^2 \cdot \sum_x \widetilde{e_B}(x)^2}} \quad (1)$$

where $\widetilde{e_A}$ and $\widetilde{e_B}$ are the zero-meaned elevation profiles of passes A and B respectively and τ is the lag (displacement) in metres. The NCC coefficient ranges from −1 to 1, with a value of 1 indicating perfect correlation between profiles at a given lag.

The NCC was evaluated over a range of along-track offsets, and the offset corresponding to the maximum correlation was taken as the best-fit local displacement between the two observations.

The search range was set dynamically, considering that the expected displacement varies with different positions on the ice shelf. The algorithm processes segments starting from the most inland segment. For this first segment, the search interval for the lag τ is defined as:

$$\tau \in [-r_1, 0], \quad r_1 = \max\left(r_{\text{inland}}, n_{cycle} \cdot r_{\text{step}}\right) \quad (2)$$

where r_{inland} provides a minimum search width, r_{step} denotes the search with the expected displacement over longer time intervals, and n_{cycle} is the number of 91-day orbit cycles between the two passes. The search interval is constrained to non-positive lags ($\tau \leq 0$), as pass B is the later pass and its features must lie downstream of those in pass A along the direction of ice flow.

For each subsequent segment, the search range is determined adaptively, based on the offset $\hat{\tau}_{\text{prev}}$ of the most recently trusted segment (defined as one with NCC peak $\geqslant$ 0.5). Since adjacent segments are expected to share similar offsets, centring the search on $\hat{\tau}_{\text{prev}}$ allows a much narrower search range to be used, reducing the likelihood of false NCC peaks arising from random correlations at unrealistic large lags. The search interval here is defined as:

$$\tau \in \left[\hat{\tau}_{\text{prev}} - r_2, \hat{\tau}_{\text{prev}} + r_2\right], \quad r_2 = n_{cycle} \cdot r_{\text{adj}} \quad (3)$$

https://doi.org/10.5194/egusphere-2026-6522
Preprint. Discussion started: 19 November 2026
© Author(s) 2026. CC BY 4.0 License.

where r_{adj} reflects the maximum possible offset difference between adjacent segments. If a segment gets an NCC peak below 0.5, its offset is not propagated and the most recently trusted offset is retained as the search centre for the next segment. In this study, the following parameter values were used: $r_{inland} = 500\,m$, $r_{step} = 100\,m$, and $r_{adj} = 100\,m$.

3.2.3 Fracture Pair Assignment

Following the NCC analysis, the estimated along-track displacement for each segment was used to predict the position of each fracture between repeat observations. For each fracture detected in pass B, its expected position in pass A was determined by applying the NCC-derived segment displacement at the fracture centre latitude. Fractures detected in pass A located within a predefined tolerance window of this predicted position were identified as candidate matches. Each candidate pair was then evaluated according to the geometric similarity of the two fractures.

The similarity between candidate fracture pairs was quantified using a weighted score based on four geometric criteria: (1) the distance between fracture centres, where the fracture centre is defined as the midpoint of the pour surface, d_{centre}); (2) the distance between the deepest points (d_{min}); (3) the relative difference in fracture depth (Δh_{rel}); and (4) the relative difference in fracture width (Δw_{rel}). These criteria jointly assess the consistency of fracture position, shape, and size between the two observations. The positional distance was defined as:

$$d_{pos} = min(|d_{centre}|, |d_{min}|) \tag{4}$$

taking the smaller of the two as a robust measure of positional similarity. The relative difference in fracture depth and width was defined as:

$$\Delta h_{\mathrm{rel}} = \frac{|h_A - h_B|}{\max(h_A, h_B)} \tag{5}$$

$$\Delta w_{\mathrm{rel}} = \frac{|w_A - w_B|}{\max(w_A, w_B)} \tag{6}$$

where h_A, h_B, w_A, w_B denote the depth and width of the fractures in pass A and B respectively.

Following that, the full scoring function for fracture matching is:

$$S = w_d \cdot \frac{d_{\mathrm{pos}}}{\varepsilon_{\mathrm{pos}}} + w_h \cdot \frac{\Delta h_{\mathrm{rel}}}{\varepsilon_h} + w_w \cdot \frac{\Delta w_{\mathrm{rel}}}{\varepsilon_w} \tag{7}$$

where w_d, w_h and w_w are the weights of the three components. S denotes the overall score. $\varepsilon_{\mathrm{pos}}$, ε_{h} and ε_w are the tolerances that scale with the number of orbit cycles n_{cycle} between the two passes, allowing less strict matching criteria for longer time intervals. Each tolerance follows the same general form:

$$\varepsilon_x = \min\left(n_c \cdot \varepsilon_{x,\mathrm{step}},\, \varepsilon_{x,\mathrm{max}}\right) \tag{8}$$

where $x \in \{\mathrm{pos}, h, w\}$ denotes the positional, depth, and width tolerances respectively. $\varepsilon_{x,\mathrm{step}}$ controls how much the tolerance grows per cycle, and $\varepsilon_{x,\mathrm{max}}$ sets the upper limit of the tolerance.

https://doi.org/10.5194/egusphere-2026-6522
Preprint. Discussion started: 19 November 2026
© Author(s) 2026. CC BY 4.0 License.

A candidate pair was first accepted as a match if $S < S_{thres}$. If multiple candidate pairs satisfied this threshold for a given fracture in another pass, the pair with the lowest score (i.e., the most similar match) was selected, and each fracture in both passes was assigned to at most one counterpart. The fracture IDs of the matched pairs were recorded for further analysis.

The following parameter values were used: $\varepsilon_{\mathrm{pos,step}} = 200\ m$, $\varepsilon_{\mathrm{pos,max}} = 2000\ m$, $\varepsilon_{\mathrm{h,step}}, \varepsilon_{\mathrm{w,step}} = 0.5$, $\varepsilon_{\mathrm{h,max}}, \varepsilon_{\mathrm{w,max}} = 0.5$, and S_{thres} is 0.5. An example output of this algorithm is illustrated as Figure 5.

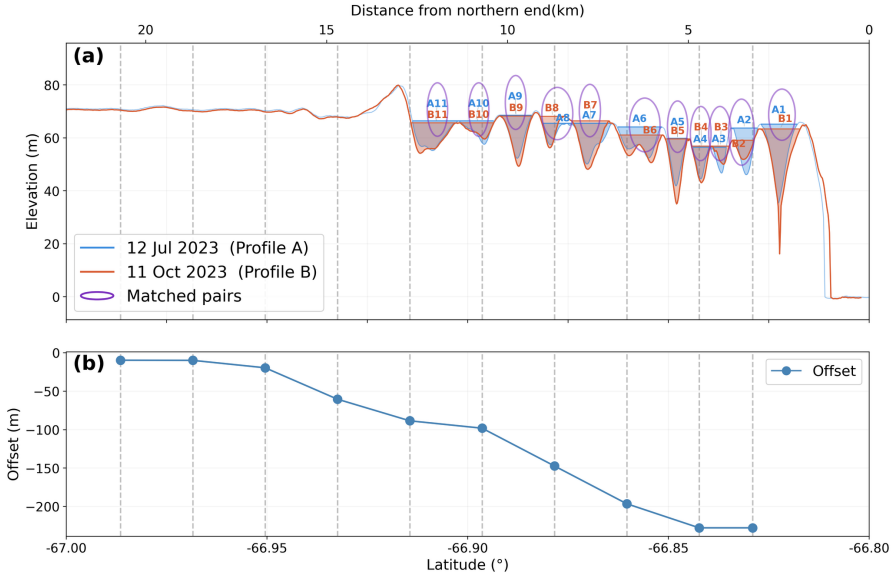


Figure 5. Example output of the NCC-based fracture matching algorithm applied to ICESat-2 track 0346, beam gt2l, for two acquisitions separated by one 91-day repeat cycle: 23 July 2023 (blue, referred to as profile A) and 11 October 2023 (red, referred to as profile B). (a) Along-track elevation profiles and fracture matching results after applying the segment-wise optimal offset. The blue profile remains fixed, while the red profile is shifted according to the estimated offset at each segment, aligning the two profiles for fracture comparison. Matched fracture pairs are indicated by purple ellipses enclosing the paired fracture labels. Vertical dashed grey lines mark the midpoint of each segment. (b) The along-track distribution of the optimal offset estimated for each segment, reflecting the spatial variation in ice displacement between the two acquisitions.

3.3 Statistical Analysis of Calving-Precursor Fracture Characteristics

To quantitatively evaluate whether fracture characteristics differed between calving-precursor and non-calving fractures, two complementary statistical analyses were performed for D/F and D/W. First, one-sided Mann-Whitney U tests were used to test the hypothesis that calving-precursor fractures have larger D/F and D/W values

https://doi.org/10.5194/egusphere-2026-6522
Preprint. Discussion started: 19 November 2026
© Author(s) 2026. CC BY 4.0 License.

than non-calving fractures. The Mann-Whitney U test is a non-parametric test that does not require the data to follow a normal distribution and is therefore suitable for comparing fracture-characteristic distributions that may be non-normal or skewed.

Second, receiver operating characteristic (ROC) analysis was used to evaluate the ability of D/F and D/W to discriminate between calving-precursor and non-calving fractures. ROC curves were generated by varying the classification threshold and plotting the resulting true positive rate (sensitivity) against the false positive rate (1 - specificity). The area under the ROC curve (AUC) was used as a summary measure of discrimination, with AUC = 1 indicating perfect discrimination and AUC = 0.5 indicating performance equivalent to random classification. For each parameter, the optimal classification threshold was determined using the Youden index, defined as the maximum value of sensitivity + specificity -1.

Calving-precursor fractures were defined as fractures manually identified as subsequently contributing to a calving event, following the procedure described in Section 4.3. Non-calving fractures comprised all other detected fractures from the same ICESat-2 tracks and observation dates, located within 20 km of the calving front and excluding fractures already identified as calving-precursor fractures. Restricting both groups to the same tracks, observation dates, and spatial domain minimised differences in sampling conditions between the two populations.

4. Results

4.1 Fracture Variability on Totten Ice Shelf

Fracture characteristics were mapped across the calving-front region of Totten Ice Shelf from October 2018 to December 2025 using the fracture-detection approach described in Section 3.1. Because ICESat-2 provides discrete along-track sampling rather than continuous spatial coverage (Fig. 1b), detected fractures were aggregated into regular grid cells following Wang et al. (2025). A 2 × 2 km grid was used to produce a multi-year map, while a coarser 3 × 3 km grid was used for annual maps to account for the lower number of observations available within individual years. For each grid cell, either the maximum or mean value of the fracture characteristic was calculated. The maximum D/F value was used to preserve the most deeply penetrating fracture within each cell, whereas the mean D/W was used to represent the typical fracture morphology within the cell.

Figure 6 shows the spatial distribution of D/F and D/W over the full study period. D/F exhibits a pronounced spatial pattern, with the highest values concentrated near the calving front. In particular, high D/F values occur in frontal areas connected to the basal channels CH1, CH2 and CH3, as well as along the inland extensions of the channel-related flow corridors CH4 and CH5 (Fig. 6a). These high-value regions extend further inland than adjacent areas without a direct channel connection. A broad region immediately east of CH1 and a smaller area near the eastern margin of the ice shelf also exhibit relatively high D/F values. In contrast, D/F is substantially lower between the major channels. Within the area delineated by the yellow box, values are generally 0.4-0.7 east of CH1 and west of CH3, compared with ~ 0.2–0.4 between CH2 and CH3 and generally below 0.3 between CH1

https://doi.org/10.5194/egusphere-2026-6522
Preprint. Discussion started: 19 November 2026
© Author(s) 2026. CC BY 4.0 License.

and CH2. Fractures become increasingly sparse upstream towards the grounding line and are largely absent across the grounded ice.

The spatial distribution of D/W broadly resembles that of D/F (Fig. 6b), with elevated values concentrated in frontal regions connected to CH1 - CH3 and along the inland extensions of CH4 and CH5. High values are also observed east of CH1 and near the eastern margin. However, several differences are evident. In particular, the region between CH2 and CH3 exhibits D/W values comparable to those observed east of CH1 and west of CH3, despite showing substantially lower D/F values. In addition, relatively high D/W values occur both upstream and downstream of the grounding line, where D/F values are comparatively low.

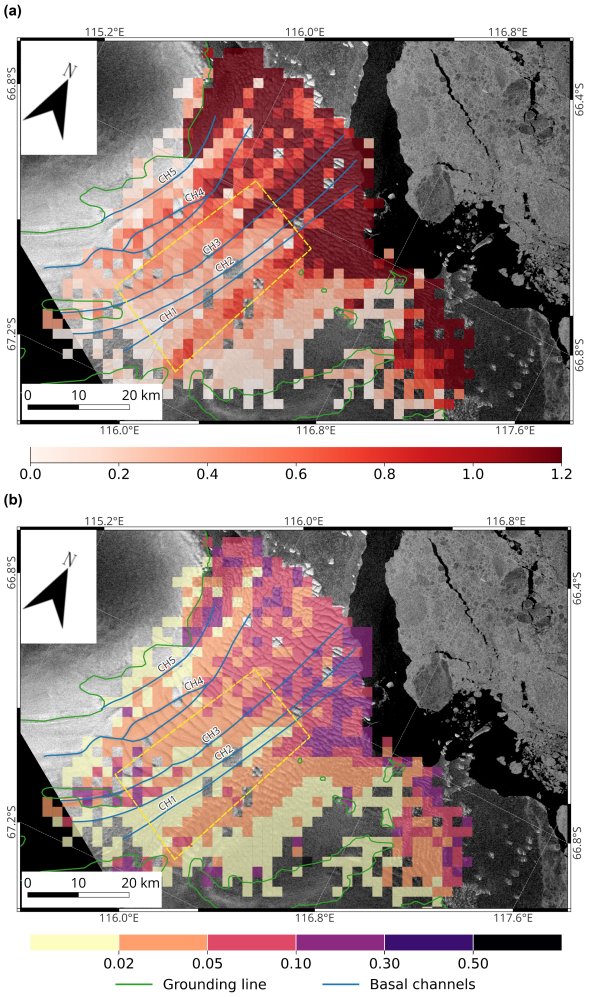


Figure 6. (a) Spatial distribution of the maximum D/F of fractures detected on Totten Ice Shelf from October 2018 to December 2025, aggregated into 2 km × 2 km grid cells. (b) As in (a) but showing the mean D/W. The background imagery of both (a) and (b) is a Sentinel-1 image with HH Polarization acquired on 24 December

https://doi.org/10.5194/egusphere-2026-6522
Preprint. Discussion started: 19 November 2026
© Author(s) 2026. CC BY 4.0 License.

2021. The solid green line denotes the grounding line from MEaSUREs dataset (Mouginot et al., 2017). The dashed yellow box represents the region encompassing the three basal channels, the fracture distribution of which is examined in detail in Figure 7. Solid blue lines indicate the approximate positions of the basal channels visible in Sentinel-1 image acquired on 24 December 2021, as validated against Lilien et al. (2025).

Figure 7 provides a higher-resolution view of the region between CH1, CH2, and CH3. The distribution of individual detected fractures reveals a pronounced spatial discontinuity between CH1 and CH2 (Fig. 7a and 7b). Fracture detections are sparse within this region, whereas fractures occur continuously between CH2 and CH3 and west of CH3. The corresponding elevation profiles (Fig. 7c–f) show that the CH1–CH2 region has relatively low surface variability and remains largely free of fractures throughout the observation period. The positions and geometries of CH1 and CH2 themselves also remain relatively stable between observations.

In contrast, the region between CH2 and CH3 contains a greater number of fractures and shows increasing surface variability towards the calving front (Fig. 7c-f). Many of these fractures are relatively shallow, consistent with low D/F values (Fig. 6a), but have comparatively high D/W ratios, indicating that they are narrow relative to their depth (Fig. 6b). West of CH3, fracture density and surface elevation variability increase substantially. Several deep fractures appear immediately east of CH3 in the profiles closest to the calving front (Fig. 7e - f), corresponding to the high D/F values observed in this region. East of CH1, fracture density and elevation variability are similarly high, although a short region of relatively smooth surface occurs between CH1 and the onset of dense fracturing. Fracture depth increases towards the calving front in both regions.

https://doi.org/10.5194/egusphere-2026-6522
Preprint. Discussion started: 19 November 2026
© Author(s) 2026. CC BY 4.0 License.

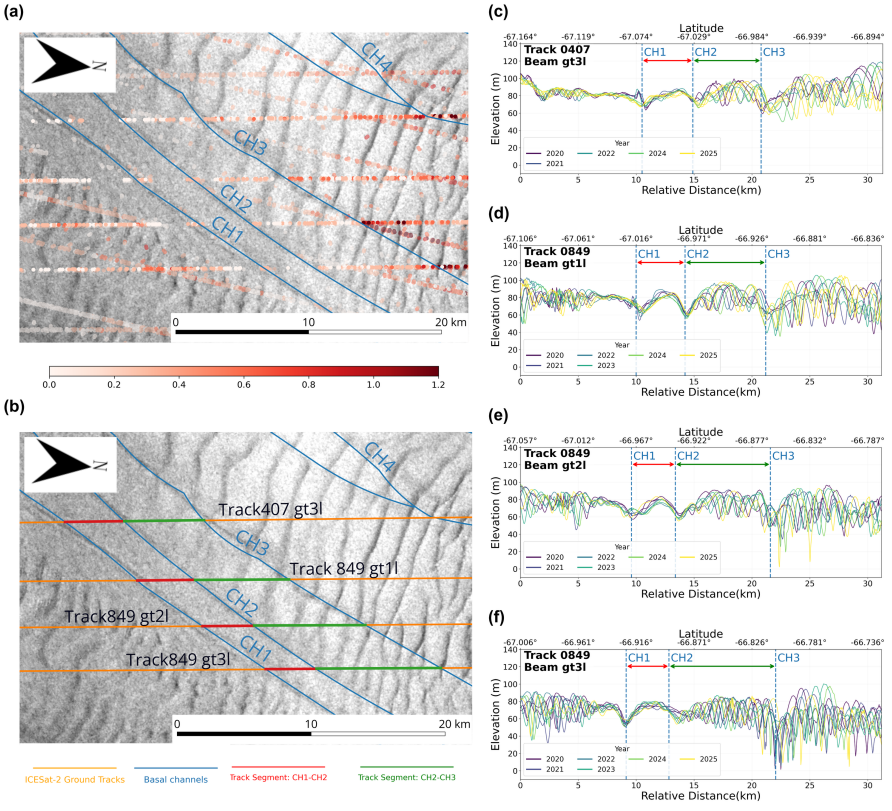


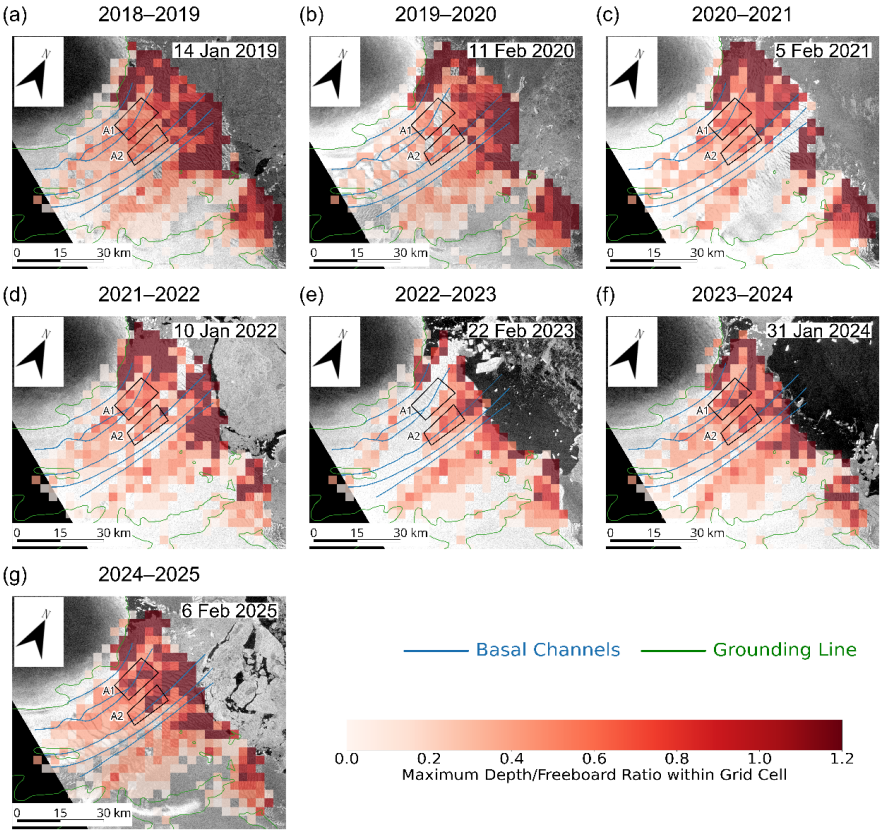
Figure 7. (a) Enlarged view of the dashed yellow box region in Figure 6, showing all fractures detected on Totten Ice Shelf from 2018 to 2025 as scatter points coloured by D/F. Four ICESat-2 beams of interest are highlighted with full opacity, while all other scatter points are shown at reduced opacity. (b) The four highlighted beams shown as solid orange lines, corresponding to the highlighted scatter points in (a): gt3l of Track 407, and gt1l, gt2l and gt3l of Track 849. These beams were selected because they provide continuous along-track coverage across the CH1–CH2 and CH2–CH3 inter-channel regions. Segments of each beam traversing the inter-channel regions are colour-coded: red indicates the segment between CH1 and CH2, and green indicates the segment between CH2 and CH3. (c)–(f) Along-track ICESat-2 elevation profiles for gt3l of Track 407 and gt1l, gt2l and gt3l of Track 849, respectively, showing all high-quality observations from 2020 to 2025. Blue dashed vertical lines indicate the approximate positions of CH1, CH2 and CH3. Red and green double-headed arrows indicate the inter-channel regions between CH1–CH2 and CH2–CH3, respectively.

The annual distributions of maximum D/F and mean D/W are shown in Figures 8 and 9 respectively. Annual maps were defined from October to September of the following year, with observations after September 2025 excluded. The annual D/F distributions retain the major spatial patterns identified in the multi-year map (Fig. 6a), with consistently higher values in frontal areas connected to the basal channels and particularly high values east of CH3. The CH1-CH2 region remains characterised by low D/F throughout the study period.

https://doi.org/10.5194/egusphere-2026-6522
Preprint. Discussion started: 19 November 2026
© Author(s) 2026. CC BY 4.0 License.

The annual maps also show a temporal cycle in frontal D/F. Extensive areas with D/F approaching or exceeding 1 are present during 2021-2022 (Fig. 8d), followed by a marked reduction in high D/F areas after the subsequent calving event (Fig. 8e). High D/F areas then expand again during 2023–2025 (Fig. 8f and 8g). A similar temporal pattern is evident in the annual D/W distributions (Fig. 9), although the spatial and temporal changes are less pronounced than for D/F.

Two inland regions labelled A1 and A2 in Figure 8 show a distinct temporal evolution. D/F in both regions increases substantially from 2022 onwards, relative to neighbouring areas at comparable along-flow distances from the calving front. The increase is particularly pronounced during 2024–2025, when some grid cells in A1 and A2 exhibit D/F values comparable to or greater than those in parts of the frontal region (Fig. 8). D/W shows a similar increase in these regions from 2023 onwards, indicating an increasing concentration of relatively narrower fractures (Fig. 9). These changes identify A1 and A2 as regions of increasing fracture activity during the latter part of the study period.



https://doi.org/10.5194/egusphere-2026-6522
Preprint. Discussion started: 19 November 2026
© Author(s) 2026. CC BY 4.0 License.

Figure 8. Spatial distribution of the maximum depth-to-freeboard ratio (D/F) of fractures detected on Totten Ice Shelf for seven annual periods from 2018 to 2025, aggregated into 3 km × 3 km grid cells. Each panel represents one annual period (October to September), labelled by the corresponding year range. The date shown in the upper right corner of each panel indicates the acquisition date of the Sentinel-1 SAR background image. The solid green line denotes the grounding line (Mouginot et al., 2017). Solid blue lines indicate the approximate positions of the basal channels visible in Sentinel-1 image acquired on 24 December 2021. The areas of interest for the analysis are denoted by two black bounding boxes, labelled A1 and A2

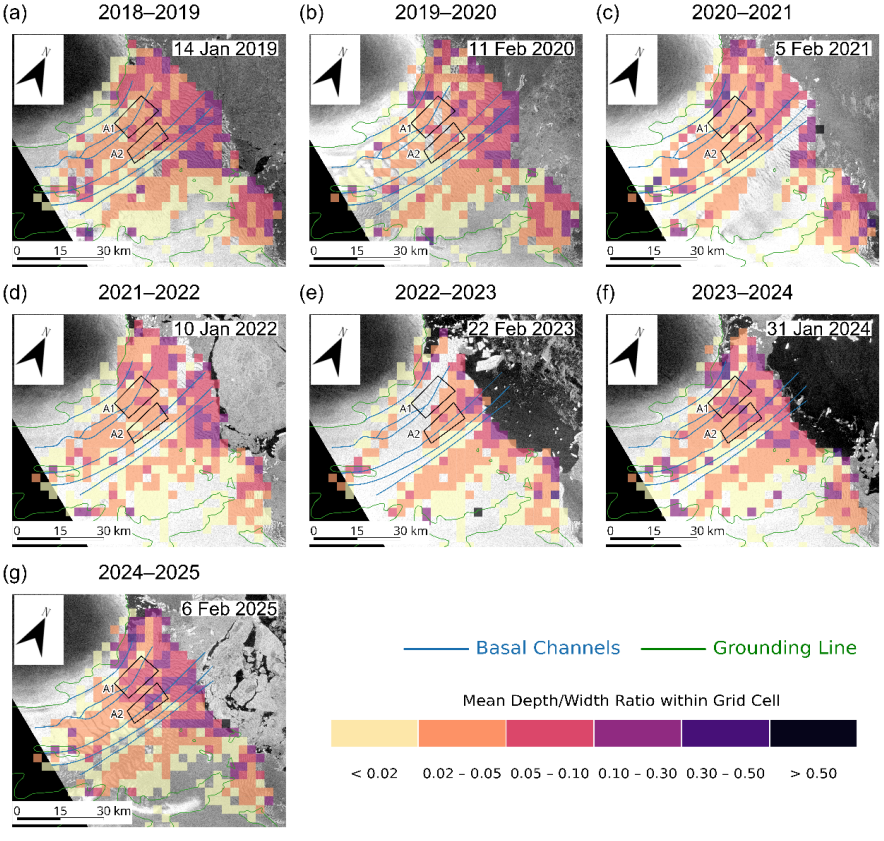


Figure 9. As in Figure 8, but showing the mean gridded depth-to-width ratio (D/W) for seven annual periods from 2018 to 2025.

4.2 Case Study of One Major Calving Event and Fracture Evolution

A major calving event occurred between 1 and 8 January 2026 and removed ~ 134.51 km² from the Totten Ice Shelf (yellow area in Fig. 10a). This was the third-largest calving event identified between October 2018 and April 2026. The two larger events occurred in 2022, but the limited repeat-track ICESat-2 observations immediately

https://doi.org/10.5194/egusphere-2026-6522
Preprint. Discussion started: 19 November 2026
© Author(s) 2026. CC BY 4.0 License.

preceding those events prevented a comparable reconstruction of fracture evolution. The January 2026 event was therefore selected as the primary case study. The three largest calving events identified during the study period are summarised in Table 1.

Table 1. Summary of the three major calving events identified on Totten Ice Shelf during the study period. Detection windows start and end dates correspond to the last Sentinel-1 image before and the first Sentinel-1 image after the calving event, respectively. Calving location indicates the approximate along-front extent with reference to basal channel positions. Calved area was derived from differencing sequential Sentinel-1 imagery.

Calving ID	Detection Window (Start)	Detection Window (End)	Calving Location	Calved Area (km²)
1	9 July 2022	16 July 2022	CH1 to CH4	169.18
2	8 Oct 2022	10 Oct 2022	East of CH1 to CH4	162.55
3	1 Jan 2026	8 Jan 2026	CH2 to CH4	134.51

The fracture associated with the 2026 event, hereafter F1, was tracked through repeated ICESat-2 observations from 2019 to 2025 (Fig. 10). In 2019–2020, F1 extended between CH3 and CH4. As the ice shelf advected toward the calving front, F1 became connected to a second fracture between CH1 and CH3, forming a longer continuous fracture system. Following calving after 2024, the section between CH1 and CH2 was removed, leaving a remaining fracture extending from CH2 to CH4 until the 2026 event. Despite this evolution, F1 retained a broadly consistent overall geometry as it advected towards the calving front. A persistent flexure occurred near CH3, where the fracture curved towards the calving front and formed a locally wider section (Fig. 10a and 10b).

The spatial evolution of F1 also shows a persistent relationship with the basal channels. The western terminus of the tracked fracture consistently coincided with CH4, whereas its eastern terminus occurred at CH3, CH2 or CH1 depending on the stage of evolution. This pattern suggests that the lateral extent of F1 remained closely associated with the channel locations throughout the observation period. The observations therefore suggest that the basal channels may have influenced the spatial development and propagation of the fracture.

Track 0582 provided repeated observations of F1 from six ICESat-2 beams. To avoid visual overlap in Figure 10b, only gt1l, gt2l and gt3l are shown because adjacent beams within each beam pair are separated by only ~ 90 m. These three beams sampled different sections of F1: gt3l crossed the section west of CH3, gt2l crossed the section adjacent to CH3, and gt1l crossed the section east of CH3. The resulting profiles provide observations of the fracture at different positions along its length and through successive stages of its evolution.

https://doi.org/10.5194/egusphere-2026-6522
Preprint. Discussion started: 19 November 2026
© Author(s) 2026. CC BY 4.0 License.

Figure 10c shows the corresponding along-track elevation profiles, centred on the fracture to facilitate comparison of its vertical morphology through time. Along gt1l, F1 first appears as a shallow depression on 4 November 2019 and progressively deepens as it approaches the calving front, while its width remains relatively stable during the early stages. After 25 July 2024, the fracture deepens substantially and develops a narrow section extending towards sea level. At the same time, the surface of the calving-front side of the fracture progressively decreases in elevation relative to the inland side. Along gt2l, F1 is initially deeper than at gt1l and reaches near-sea-level penetration by 28 July 2023, after which the fracture progressively widens. A similar lowering of the calving-front side occurs throughout this period. Along gt3l, the fracture profile changes relatively little between November 2019 and July 2023, before deepening substantially after July 2024 and approaching sea level. At the same time, the fracture widens and the calving-front side continues to lower.

Together, the three profiles reveal a consistent sequence of pre-calving geometric evolution. F1 initially develops a relatively shallow fracture and subsequently undergoes progressive deepening. Once the fracture approaches sea level, widening becomes increasingly evident, particularly in the sections monitored by gt2l and gt2r. Throughout the later stages, the calving-front side of the fracture progressively lowers relative to the inland side. Thus, the observations indicate a transition from deepening-dominated fracture growth to widening following near-sea-level penetration.

Figure 10d quantifies this evolution using D/F, D/W and W. Prior to the January 2026 calving event, D/F approached 1.0 along all six beams. At gt2l and gt2r, which sampled the section adjacent to CH3, D/F increased rapidly from ~ 0.6 to near 1.0 in July 2023 and subsequently remained close to this value. At other beam locations, D/F reached similarly high values later, primarily during 2025.

The evolution of D/W further distinguishes the two stages of fracture development. At gt2l and gt2r, D/W initially increased until July 2023 and subsequently decreased as the fracture widened after approaching sea level. At the other beam locations, D/W generally increased throughout the observation period, indicating that fracture deepening initially outpaced widening. These trends are consistent with the elevation profiles in Figure 10c.

The evolution of W provides further evidence for this transition. At gt2l and gt2r, W decreased during the initial deepening phase and increased after D/F approached 1.0. At the other beam locations, W remained relatively stable initially, decreased as the fracture deepened, and subsequently increased near the end of the observation period. The magnitude and timing of this late-stage widening are not fully reproduced in the elevation profiles shown in Figure 10c, suggesting that the apparent abrupt increase in detected width may partly reflect limitations of the fracture detection algorithm. This issue is examined further in Section 5.4. An anomalous D/W observation at gt1l is also discussed in Section 5.4.

https://doi.org/10.5194/egusphere-2026-6522
Preprint. Discussion started: 19 November 2026
© Author(s) 2026. CC BY 4.0 License.

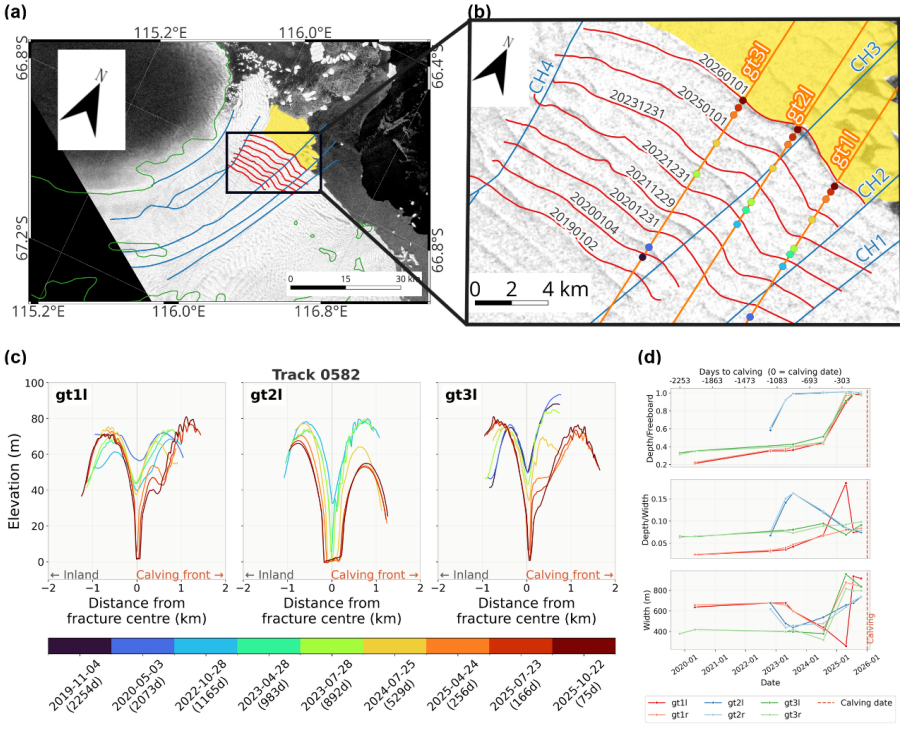


Figure 10. Case study of a major calving event and the evolution of the fracture leading to it. (a) Overview map of Totten Ice Shelf showing a calving event that occurred between 1 January and 8 January 2026. The calved area is coloured in yellow. The black bounding box indicates the region shown in detail in (b). Red lines show the evolution of the fracture F1 leading to this calving event. Blue lines represent the basal channels, and green lines represent the grounding line. The background imagery is a Sentinel-1 image acquired on 26 November 2025. (b) Detailed view of the evolution of fracture F1. Red lines with date labels show the successive positions of F1 leading up to the calving event. Orange lines are the ground tracks of beams gt1l, gt2l and gt3l of ICESat-2 track 0582. The dots indicate the locations at which F1 was detected from ICESat-2 data at different times, with dot colours corresponding to the colour bar shown in (c). (c) Evolution of F1 as observed by three beams: gt1l, gt2l and gt3l. Each profile is normalised relative to the fracture centre. The colour of each profile indicates the observation date, as labelled on the colour bar. (d) Three characteristics of F1 derived from all six beams of track 0582: the depth-to-freeboard ratio (D/F), the depth-to-width ratio (D/W), and the width at three-quarter depth (W). The red dashed line indicates the calving date.

4.3 Calving-Precursor Fracture Characteristics and Their Evolution

The analysis focussed on calving-precursor fractures identified from Sentinel-1 imagery and corresponding ICESat-2 observations along seven tracks covering the eastern part of the Totten Ice Shelf (tracks 79, 346, 521, 788, 963, 1024 and 1230). For each calving event, the fracture associated with the event was identified from Sentinel-1 imagery and linked to the corresponding fracture detected in the latest available ICESat-2 observation prior to the calving event. The NCC fracture matching algorithm was then used to track the evolution of these

https://doi.org/10.5194/egusphere-2026-6522
Preprint. Discussion started: 19 November 2026
© Author(s) 2026. CC BY 4.0 License.

fractures through time. Only fractures with at least three valid observation dates were retained for the temporal analysis. The resulting distributions of fracture characteristics and their comparison with non-calving fractures are shown in Figure 11, while the temporal evolution of D/F is shown in Figure 12.

For the comparison in Figure 11, non-calving fractures were selected from the same tracks and observation dates as the calving-precursor fractures and restricted to within 20 km of the calving front. Both D/F and D/W are significantly higher for calving-precursor fractures than in non-calving fractures (one-sided Mann-Whitney U test, $p < 0.001$ for both parameters). The median D/F is 0.924 for calving-precursor fractures compared with 0.317 for non-calving fractures, while the corresponding median D/W values are 0.095 and 0.040 respectively. The difference is more pronounced for D/F which has an ROC AUC of 0.832 compared with 0.734 for D/W. The Youden-index threshold of D/F = 0.618, and the classification achieves a sensitivity of 76.5% and a specificity of 80.0%.

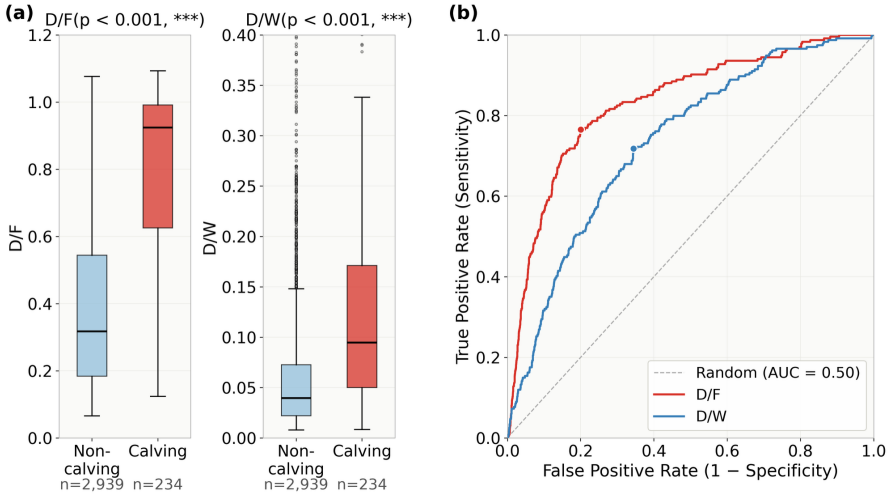


Figure 11. Comparison of fracture characteristics between calving and non-calving fractures, and their ability to distinguish calving events. (a) Box plots showing the distribution of D/F (left) and D/W (right) for non-calving fractures (blue) and calving fractures (red). The horizontal black line inside each box shows the median. The box spans the interquartile range (Q1 to Q3), and the whiskers extend to 1.5 times the interquartile range. Points beyond the whiskers are shown as individual outliers. (b) ROC curves for D/F (red) and D/W (blue), showing the trade-off between true positive rate and false positive rate at different classification thresholds. The grey dashed line represents random classification (AUC = 0.50). Filled circles indicate the optimal threshold for each parameter based on the maximum Youden index.

More than half of the calving-precursor fractures exhibit an increasing D/F trend prior to calving, and most reach values approaching 1.0 at or shortly before the associated calving event (Fig. 12). Two distinct evolutionary patterns are evident among fractures with increasing D/F. In the first, D/F begins at relatively low values of ~ 0.2–0.4 and increases progressively towards 1.0, similar to the evolution observed for F1 in Section 4.2. In the second,

https://doi.org/10.5194/egusphere-2026-6522
Preprint. Discussion started: 19 November 2026
© Author(s) 2026. CC BY 4.0 License.

D/F is already high, typically 0.8–1.0, several hundred days before calving and subsequently increases only slightly or remains approximately stable. Thus, although the timing and rate of D/F increase vary substantially between fractures, elevated D/F is generally observed during the final stages preceding calving.

A smaller number of fractures maintain relatively low D/F values close to the calving date, while ten cases exhibit an overall decrease in D/F during the observation period. These anomalous trends may reflect spatial sampling effects associated with the along-track geometry of ICESat-2 observations. Because fracture morphology can vary considerably along its length, repeat ICESat-2 tracks may sample different portions of a migrating fracture as the ice shelf flows. The implications of this sampling effect are considered further in Section 5.4.

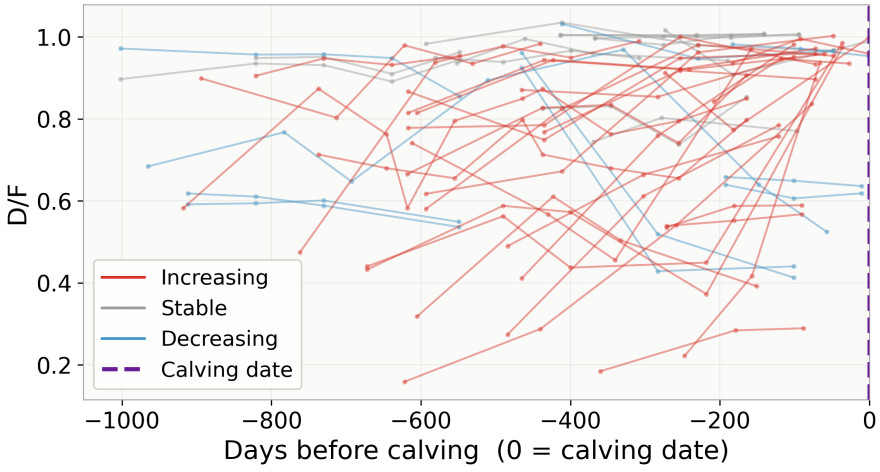


Figure 12. Time series of D/F for calving-precursor fractures. The purple dashed line indicates the calving date. Solid lines show the evolution of individual fracture chains, coloured by their overall trend: red lines indicate fractures with a generally increasing D/F, blue lines indicate a decreasing trend, and grey lines indicate a stable trend. Trend classification is based on the normalised slope of the time series: values greater than 0.0001 day^{-1} are classified as increasing, values less than −0.0001 day^{-1} as decreasing, and values within this range as stable.

5. Discussion

5.1 Spatial Controls on Fracture Distribution: Role of Basal Channels

One of the strongest spatial patterns identified in this study is the concentration of high D/F values in frontal areas associated with basal channels, particularly CH1, CH2, and CH3 (Fig. 6). Several processes may contribute to this pattern. First, basal channels are associated with enhanced basal melting driven by the circulation of relatively warm ocean water beneath the ice shelf base, producing localised thinning and potentially weakening the overlying ice (Alley et al., 2016). Basal channels also generally deepen in the downstream direction (Alley et al., 2016), such that channel-connected frontal regions may experience greater basal thinning and associated structural weakening than more inland portions of the same flow corridors. These processes provide a plausible explanation

https://doi.org/10.5194/egusphere-2026-6522
Preprint. Discussion started: 19 November 2026
© Author(s) 2026. CC BY 4.0 License.

for the concentration of deep fractures and high D/F values observed near the channel-connected ice shelf front. The persistent polynya identified at the Totten ice front by Alley et al (2016) provides independent evidence for active ocean-water exchange within the channel system and supports the interpretation that basal melting remains an important process in these regions.

A second factor may be the reduction in lateral buttressing seaward of pinning points in the eastern part of CH1. Notably, the inland extent of elevated D/F along the channel approximately coincides with the along-flow position of the pinning point, suggesting that lateral confinement provided by the pinning points may limit fracture development upstream of this location. This interpretation is consistent with Dow et al. (2018), who showed that fractures on Totten Ice Shelf are associated with regions of active frontal calving after the ice shelf became unpinned from grounded areas along its margins. Thus, the spatial distribution of fracture damage may reflect the combined effects of basal thinning and the progressive reduction of lateral mechanical restraint towards the calving front.

A particularly distinctive feature of the fracture distribution is the region between CH1 and CH2. Here, D/F remains consistently low, generally below 0.3, while the surface elevation profiles show substantially less fracture activity and temporal variability than neighbouring regions (Fig. 6 and 7). The persistence of this low-fracture zone suggests that its behaviour may differ mechanically from that of the surrounding ice. One possible analogue is the suture zones observed on Larsen C Ice Shelf, where fractures commonly terminate upon encountering regions of material heterogeneity (McGrath et al., 2014). In Larsen C, suture zones contain relatively soft marine ice, but their higher fracture toughness can allow them to inhibit fracture propagation despite their lower inferred stiffness (McGrath et al., 2014).

A similar mechanism may operate in the CH1–CH2 region. Basal channels can be associated with marine-ice formation within the ice shelf, as inferred from thermodynamic modelling (Le Brocq et al., 2013) and supported by radar observations elsewhere on Antarctic ice shelves (Whiteford et al., 2022). The inter-channel region between CH1 and CH2 may therefore contain material contrasts that influence fracture propagation. The geometry of this region also finds a potential structural analogue in the Larsen C Suture zones, which develop between neighbouring meteoric-ice inflows and are associated with contrasting ice thickness, flow convergence, and ice mélange (McGrath et al., 2014). On Totten Ice Shelf, the CH1–CH2 region lies between major basal channels associated with distinct upstream flow tributaries and convergent flow (Lilien et al., 2025), potentially creating similarly heterogenous structural conditions.

The observed fracture distribution is consistent with this interpretation. Fractures are sparse within the CH1–CH2 region and frequently terminate at the boundaries of the basal channels, as illustrated by F1 in Figure 7. Other channels, including CH3 and CH4, may also act as preferential boundaries to fracture propagation although their apparent influence is weaker because some fractures extend across these channels. The CH1–CH2 region may therefore exhibit suture-zone-like behaviour, inhibiting fracture development relative to the surrounding ice. However, this interpretation remains a hypothesis. Direct radar evidence for marine ice or other material contrasts within the CH1–CH2 region is not available from this study, and it is therefore not possible to determine whether

https://doi.org/10.5194/egusphere-2026-6522
Preprint. Discussion started: 19 November 2026
© Author(s) 2026. CC BY 4.0 License.

the observed fracture termination is primarily controlled by material heterogeneity, spatial variations in the stress field, or their interaction. Further geophysical observations would be required to distinguish between these mechanisms.

5.2 Fracture Evolution and Calving-Precursor Signals

The results demonstrate that the depth-to-freeboard ratio, D/F, originally proposed by Wang et al. (2025), provides a useful indicator of fracture damage and calving potential on Totten Ice Shelf. Benn et al. (2007) proposed that calving occurs when fractures penetrate through the ice shelf to sea level, corresponding to D/F approaching 1.0. Consistent with this, calving-precursor fractures in our dataset have substantially higher D/F values than non-calving fractures, and D/F provides better classification performance than D/W. The ROC analysis yields an AUC of 0.832 for D/F, compared with 0.734 for D/W with an optimal D/F threshold of 0.618. These results indicate that the vertical penetration of a fracture relative to local freeboard is more closely associated with calving potential than its width relative to depth. The threshold of 0.618 may represent a transition towards a more advanced fracture-damage state at Totten Glacier, although it should not be interpreted as a universal physical threshold.

The evolution of F1 provides further insight into how fracture damage develops prior to calving. The three sections of F1 sampled by gt1l, gt2l, and gt3l reached D/F values approaching 1.0 at markedly different times. The section sampled by gt2l, adjacent to CH3, reached near-full penetration ~ 900 days before the January 2026 calving event, whereas the gt3l and gt1l sections reached similarly high values only ~ 300 days before calving. Thus, full penetration developed progressively along the fracture rather than occurring simultaneously along its entire length. The persistence of incompletely penetrated sections for several hundred days after the first section reached near-sea-level depth indicates that penetration at a single location was not sufficient to produce the observed calving event. Instead, the January 2026 event occurred only after near-full penetration had developed along the full observed length of F1. This behaviour is consistent with the fracture-penetration criterion of Benn et al. (2007), while suggesting that the spatial continuity of fracture penetration is also important for large calving events.

The F1 profiles also reveal a distinct change in fracture morphology after near-sea-level penetration. During the initial stage, fracture depth increased while width remained relatively stable or decreased, producing increasingly narrow and deep fracture geometries. Once D/F approached 1.0, widening became more pronounced, particularly in the section adjacent to CH3. At the same time, the surface on the calving-front side of the fracture progressively lowered relative to the inland side, producing a persistent asymmetry across the fracture. Walker & Gardner (2019) documented similar offsets between the seaward and landward walls of actively propagating rifts on Antarctic ice shelves and attributed the asymmetry to the sub-vertical geometry of the rifts and the resulting imbalance in buoyancy forces between the two walls. The similar behaviour observed for F1 therefore provides evidence that the fracture remained mechanically active during the period immediately preceding calving. However, the present observations do not establish whether the asymmetric surface lowering directly promotes fracture widening or instead represents a response to ongoing fracture propagation.

https://doi.org/10.5194/egusphere-2026-6522
Preprint. Discussion started: 19 November 2026
© Author(s) 2026. CC BY 4.0 License.

The early evolution of F1 provides a further indication of how fracture damage may develop through the ice thickness. D/F remained relatively low, ~ 0.2–0.4, for several years before increasing rapidly during the final year before calving. One possible interpretation is that this prolonged shallow phase represents the surface expression of a basal crevasse that progressively propagated upward through the ice shelf. McGrath et al. (2012) showed that basal crevasses on Larsen C Ice Shelf can initially produce only weak surface deformation before developing more pronounced surface expressions as the basal fracture grows upward. The subsequent rapid increase in D/F observed for F1 would then represent the stage at which the upward-propagating basal fracture approached and connected with the surface expression. This interpretation is also consistent with the necking instability described by Bassis & Ma (2015), whereby narrow basal crevasses can undergo progressive deepening through the ice thickness as they advect downstream, with their evolution influenced by ice–ocean thermodynamic interactions. Dow et al. (2018) similarly suggested that fractures on Totten Ice Shelf may originate as basal rather than surface crevasses. Although the ICESat-2 observations cannot directly resolve the subsurface initiation of F1, its prolonged shallow phase followed by rapid deepening is consistent with this interpretation.

The broader population of calving-precursor fractures shows evolutionary behaviour that is broadly consistent with the F1 case study (Fig. 12). More than half of the tracked fractures exhibit increasing D/F before calving, while many others maintain already elevated values of ~ 0.8–1.0 throughout the available observation period. The former resembles the later evolution of the gt1l- and gt3l-monitored sections of F1, where D/F increased substantially during the period preceding calving. The latter resembles the gt2l section, which reached near-full penetration substantially earlier and remained close to D/F = 1 thereafter. These observations suggest that calving precursors do not necessarily follow a single temporal trajectory. Some fractures undergo substantial measurable damage during the available ICESat-2 record, whereas others are already highly developed when first captured. Because the temporal coverage of individual fracture tracks is limited and depends on both ICESat-2 acquisition availability and the success of NCC-based matching, it is not possible to determine whether the latter group experienced an earlier shallow-growth phase analogous to that inferred for F1.

The spatial distribution of D/F provides further evidence that the progression towards calving is spatially organised (Fig. 8). The frontal region between CH3 and CH4 is associated with all three major calving events identified during the study period (Table 1), and high D/F values repeatedly develop near these channel margins before major calving events. The F1 observations indicate that penetration can initially become advanced near the channel-associated sections of a fracture while other sections remain relatively shallow. Subsequently, the less-penetrated sections deepen, while the already penetrated sections may undergo widening. When near-full penetration extends across the full observed fracture length, the spatial distribution appears as a continuous zone of elevated D/F along the calving front. This sequence is evident before both the 2022 and 2026 major calving events and suggests that the spatial continuity of high D/F may provide a useful precursor signal.

Two potential pre-calving signals can therefore be identified in the annual D/F maps (Fig. 8). The first is the development of localised high D/F adjacent to CH3 and CH4, particularly within areas A1 and A2. The second is the subsequent development of a more continuous zone of elevated D/F along the frontal fracture system. The latter pattern is particularly clear during 2024–2025 and spatially corresponds to the region involved in the January

https://doi.org/10.5194/egusphere-2026-6522
Preprint. Discussion started: 19 November 2026
© Author(s) 2026. CC BY 4.0 License.

2026 calving event. The recurrence of these patterns suggests that multi-temporal D/F maps may provide a basis for identifying areas undergoing progressive fracture damage before major calving events.

The 2024–2025 distribution also indicates that elevated D/F had developed in A1 and A2 more than 10 km upstream of the then-current calving front. Because similar elevated values preceded the 2026 event, these regions may warrant particular attention in future monitoring. However, the available observations are insufficient to establish that elevated D/F in A1 and A2 will necessarily lead to another major calving event, or to predict its timing. Rather, the results demonstrate the potential of ICESat-2 D/F observations as an indicator of evolving fracture damage that could complement existing satellite-based calving monitoring.

5.3 ICESat-2 Altimetry for Ice Shelf Fracture Monitoring

Satellite remote sensing provides the primary means of monitoring ice shelf fractures over large spatial scales, with optical imagery and SAR widely used to map their surface expression. However, these observations provide limited information on their vertical structure. The results presented here show that ICESat-2 along-track altimetry complements conventional image-based observations by resolving fracture depth and geometry directly from surface-elevation profiles. In particular, the depth-to-freeboard ratio provides a quantitative measure of fracture penetration that cannot be derived directly from two-dimensional imagery. The repeat observations provided by ICESat-2 further allow changes in fracture geometry to be monitored over multi-year periods, as demonstrated by the fracture time series presented in Figures 10 and 12. The combination of ICESat-2 elevation profiles with automated fracture detection and NCC-based matching therefore provides a framework for monitoring the vertical evolution of individual fractures and relating this evolution to calving.

5.4 Limitations and future directions

The principal limitation of the approach is the temporal sampling of ICESat-2. Although the nominal repeat cycle is ~ 91 days, cloud cover and incomplete data coverage can substantially increase the interval between valid observations. This limits the ability to resolve fracture evolution immediately before individual calving events and increases the potential for uncertainty in fracture matching. In particular, when the interval between observations is long, changes in surface elevation caused by ice flow, surface processes and fracture evolution may reduce the similarity between successive profiles and increase the probability of an incorrect NCC match. Consequently, the fracture time series presented here should be interpreted as discrete observations of fracture evolution rather than continuous records of the pre-calving process.

A second limitation arises from the discrete spatial sampling of ICESat-2. Unlike satellite imagery, which can provide spatially continuous observations of the ice-shelf surface, ICESat-2 measures elevation only along individual ground tracks. Fractures that do not intersect a ground track therefore cannot be monitored using this approach. More importantly, the relationship between ground track orientation and ice flow direction can influence the consistency of fracture sampling between repeat observations. When a ground track is not closely aligned with the local flow direction, ice advection causes successive observations to intersect different along-flow positions

https://doi.org/10.5194/egusphere-2026-6522
Preprint. Discussion started: 19 November 2026
© Author(s) 2026. CC BY 4.0 License.

of the same fracture. The resulting changes in the sampled fracture cross-section may be incorrectly interpreted as temporal changes in fracture geometry.

This effect is particularly relevant to the calving-precursor time series in Figure 12. Track 0582, used for the F1 case study, is relatively well aligned with the local flow direction, reducing the positional shift between successive observations. In contrast, the seven tracks used for the broader calving-precursor analysis have different orientations relative to ice flow. The anomalous decreases in depth-to-freeboard ratio observed for some fractures may therefore result partly from different portions of the same fracture being sampled at different times, rather than from actual fracture healing or a reduction in fracture depth. This limitation highlights the importance of considering both ground-track geometry and ice-flow direction when interpreting repeat ICESat-2 measurements of individual fractures.

A third limitation is that uncertainty remains in the delineation of individual fractures. Although the algorithm successfully identifies most fractures in the along-track elevation profiles, small differences in local surface geometry between repeat observations can result in different representations of the same physical fracture. The example in Figure 13 illustrates this problem: a fracture that is identified as a single feature (F7) on 12 July 2023 is separated into three smaller features (F7–F9) on 11 October 2023 because of the hierarchical parent–child selection criteria. A similar inconsistency could contribute to anomalies such as the apparent abrupt increase in width identified for F1 in Figure 10d. Such inconsistencies highlight the sensitivity of fracture geometry to the detection thresholds and indicate that some apparent changes in fracture characteristics may reflect detection artefacts rather than physical evolution. Future work could investigate adaptive detection criteria that account for local fracture geometry and improve the consistency of fracture delineation between repeat observations.

https://doi.org/10.5194/egusphere-2026-6522
Preprint. Discussion started: 19 November 2026
© Author(s) 2026. CC BY 4.0 License.

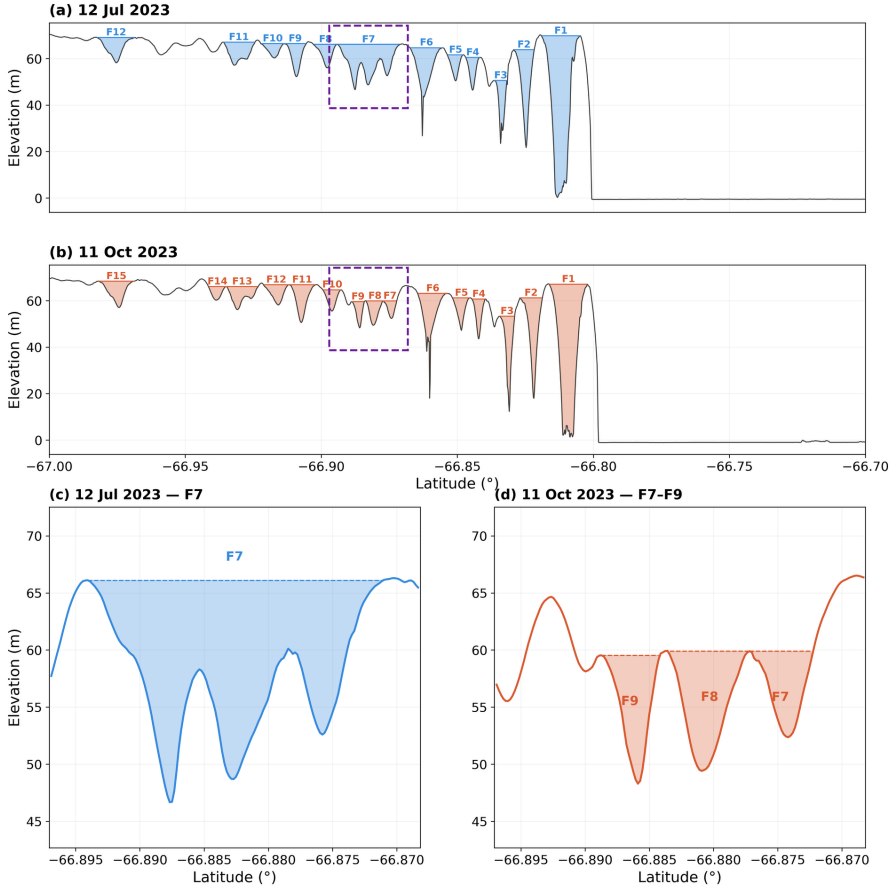


Figure 13. Comparison of fracture geometry at the same along-track location on ICESat-2 track 0346, beam gt1l, between two acquisitions separated by one 91-day repeat cycle. (a) Along-track elevation profile on 12 July 2023, with detected fractures shaded in blue. (b) Corresponding profile on 11 October 2023, with detected fractures shaded in red. The purple dashed rectangle in (a) and (b) marks the region shown in the zoomed panels. (c) Zoom-in of the F7 region on 12 July 2023, where a single fracture (F7) was detected. (d) Zoom-in of the same region on 11 October 2023, where the former single fracture had split into three smaller fractures (F7–F9).

A fourth limitation is that the identification of calving events and their associated precursor fractures relied on manual inspection of Sentinel-1 imagery. This process is time-consuming and introduces an element of observer subjectivity, and it restricted the statistical analysis of calving-precursor fractures to seven ICESat-2 tracks covering the eastern part of Totten Ice Shelf. Automated calving-front change detection could substantially expand this dataset by systematically identifying calving events, estimating their timing and area, and linking them to the corresponding ICESat-2 fracture observations. Such an expanded dataset would allow the predictive performance of the depth-to-freeboard ratio to be evaluated across a larger portion of Totten Ice Shelf and over a greater number of calving events.

https://doi.org/10.5194/egusphere-2026-6522
Preprint. Discussion started: 19 November 2026
© Author(s) 2026. CC BY 4.0 License.

Finally, the interpretation of the CH1–CH2 inter-channel region as potentially exhibiting suture zone-like behaviour remains untested. The persistent suppression of fracture development in this region is consistent with a material boundary, but the present observations cannot distinguish between control by internal material heterogeneity and variations in the local stress field. Ice-penetrating radar observations could provide a direct test of the material-heterogeneity hypothesis by determining whether marine ice or other distinctive internal structures occur within the inter-channel region. Such observations would also provide constraints on the internal geometry of the basal channels and the distribution of basal and internal fractures, providing an important subsurface perspective on the processes controlling fracture propagation on Totten Ice Shelf.

6. Conclusions

This study presents the first systematic analysis of fracture distribution, vertical structure, and temporal evolution on Totten Ice Shelf using ICESat-2 observations. A hierarchical fracture-detection approach and a novel NCC-based fracture-matching algorithm were used to extract and track individual fractures across repeat observations from 2018 to 2025.

Three main findings emerge. First, fracture characteristics show strong spatial variability, with the highest depth-to-freeboard ratios occurring predominantly in frontal areas connected to basal channels. In contrast, the inter-channel region between CH1 and CH2 consistently exhibits low fracture density and shallow fractures, suggesting the presence of a structural boundary that may be related to suture zone-like material heterogeneity. Second, the depth-to-freeboard ratio is a stronger discriminator of calving-precursor fractures than the depth-to-width ratio, indicating that fracture penetration relative to ice freeboard provides a useful measure of structural damage and calving potential. Third, analysis of fracture F1 and the broader calving-precursor dataset reveals a consistent pre-calving sequence in which deep penetration develops first near basal channels and subsequently extends along the fracture. Major calving events occur after the depth-to-freeboard ratio approaches unity along the full fracture length. The reappearance of continuous zones of high depth-to-freeboard ratio along the calving front therefore provides a potential short-term indicator of impending major calving on Totten Ice Shelf.

The NCC-based matching algorithm provides a new approach for automatically tracking individual fractures between repeat ICESat-2 observations and quantifying their geometric evolution. Despite limitations associated with ICESat-2 sampling, fracture delineation, and ATL06 resolution, the results demonstrate the potential of repeat laser altimetry for monitoring the vertical evolution of ice shelf fractures over multi-year periods. Future work should focus on higher-resolution ATL03-based processing, radar observations to test the proposed suture-zone interpretation, and integration with strain-rate fields to better constrain the mechanical controls on fracture development. Extending this framework to other Antarctic ice shelves will provide an important test of the generality of the observed fracture–calving relationships.

https://doi.org/10.5194/egusphere-2026-6522
Preprint. Discussion started: 19 November 2026
© Author(s) 2026. CC BY 4.0 License.

Code and data availability

The normalised cross-correlation (NCC) matching algorithm code and TIFF files of gridded depth/freeboard and depth/width across Totten Ice Shelf will be made available via the University of Cambridge Apollo repository on publication.

Author contributions

Both authors conceived of the work. CC developed the NCC code and performed all the analysis under the supervision of IW. CC wrote the initial draft of the manuscript, and both authors edited it to produce the final version.

Competing interests

The authors declare no competing interests

Acknowledgements

CC thanks the 2025/26 MPhil in Polar Studies cohort for their comradery and support during the year.

Financial support

This work was undertaken while IW was in receipt of the Natural Environment Research Council Pushing the Frontiers Grant (UKRI4317).

References

Aitken, A. R. A., Young, D. A., Ferraccioli, F., Betts, P. G., Greenbaum, J. S., Richter, T. G., Roberts, J. L., Blankenship, D. D., & Siegert, M. J. (2014). The subglacial geology of Wilkes Land, East Antarctica. *Geophysical Research Letters*, *41*(7), 2390–2400. https://doi.org/10.1002/2014GL059405

Alley, K. E., Scambos, T. A., Siegfried, M. R., & Fricker, H. A. (2016). Impacts of warm water on Antarctic ice shelf stability through basal channel formation. *Nature Geoscience*, *9*(4), 290–293. https://doi.org/10.1038/ngeo2675

Alley, R. B., Cuffey, K. M., Bassis, J. N., Alley, K. E., Wang, S., Parizek, B. R., Anandakrishnan, S., Christianson, K., & DeConto, R. M. (2023). Iceberg Calving: Regimes and Transitions. *Annual Review of Earth and Planetary Sciences*, *51*(Volume 51, 2023), 189–215. https://doi.org/10.1146/annurev-earth-032320-110916

Bassis, J. N., & Ma, Y. (2015). Evolution of basal crevasses links ice shelf stability to ocean forcing. *Earth and Planetary Science Letters*, *409*, 203–211. https://doi.org/10.1016/j.epsl.2014.11.003

Benn, D. I., Warren, C. R., & Mottram, R. H. (2007). Calving processes and the dynamics of calving glaciers. *Earth-Science Reviews*, *82*(3), 143–179. https://doi.org/10.1016/j.earscirev.2007.02.002

https://doi.org/10.5194/egusphere-2026-6522
Preprint. Discussion started: 19 November 2026
© Author(s) 2026. CC BY 4.0 License.



874 Breyer, C., Barcheck, G., Gomez-Fell, R., Hillebrand, T., Hills, B. H., Kaluzienski, L. M., Martin, J., Polashenski,
875 D., & Shapero, D. (2020). *Ice sheet surface velocity determination from ICESat-2 repeat tracks*. *2020*,
876 C028-0014. https://ui.adsabs.harvard.edu/abs/2020AGUFMC028.0014B

877 Cook, S., Åström, J., Zwinger, T., Galton-Fenzi, B. K., Greenbaum, J. S., & Coleman, R. (2018). Modelled
878 fracture and calving on the Totten Ice Shelf. *The Cryosphere*, *12*(7), 2401–2411.
879 https://doi.org/10.5194/tc-12-2401-2018

880 Davison, B. J., Hogg, A. E., Slater, T., Rigby, R., & Hansen, N. (2025). Antarctic Ice Sheet grounding line
881 discharge from 1996–2024. *Earth System Science Data*, *17*(7), 3259–3281.
882 https://doi.org/10.5194/essd-17-3259-2025

883 Depoorter, M. A., Bamber, J. L., Griggs, J. A., Lenaerts, J. T. M., Ligtenberg, S. R. M., van den Broeke, M. R.,
884 & Moholdt, G. (2013). Calving fluxes and basal melt rates of Antarctic ice shelves. *Nature*, *502*(7469),
885 89–92. https://doi.org/10.1038/nature12567

886 Dow, C. F., Lee, W. S., Greenbaum, J. S., Greene, C. A., Blankenship, D. D., Poinar, K., Forrest, A. L., Young,
887 D. A., & Zappa, C. J. (2018). Basal channels drive active surface hydrology and transverse ice shelf
888 fracture. *Science Advances*, *4*(6), eaao7212. https://doi.org/10.1126/sciadv.aao7212

889 Dupont, T. K., & Alley, R. B. (2005). Assessment of the importance of ice-shelf buttressing to ice-sheet flow.
890 *Geophysical Research Letters*, *32*(4). https://doi.org/10.1029/2004GL022024

891 Gorelick, N., Hancher, M., Dixon, M., Ilyushchenko, S., Thau, D., & Moore, R. (2017). Google Earth Engine:
892 Planetary-scale geospatial analysis for everyone. *Remote Sensing of Environment, Big Remotely Sensed*
893 *Data: Tools, Applications and Experiences*, *202*, 18–27. https://doi.org/10.1016/j.rse.2017.06.031

894 Greenbaum, J. S., Blankenship, D. D., Young, D. A., Richter, T. G., Roberts, J. L., Aitken, A. R. A., Legresy, B.,
895 Schroeder, D. M., Warner, R. C., van Ommen, T. D., & Siegert, M. J. (2015). Ocean access to a cavity
896 beneath Totten Glacier in East Antarctica. *Nature Geoscience*, *8*(4), 294–298.
897 https://doi.org/10.1038/ngeo2388

898 Gwyther, D., Galton- Fenzi, B.K., & Williams, G.D. (2011). Model simulations investigate Totten thinning.
899 https://api.semanticscholar.org/CorpusID:130305205.

900 Le Brocq, A. M., Ross, N., Griggs, J. A., Bingham, R. G., Corr, H. F. J., Ferraccioli, F., Jenkins, A., Jordan, T.
901 A., Payne, A. J., Rippin, D. M., & Siegert, M. J. (2013). Evidence from ice shelves for channelized
902 meltwater flow beneath the Antarctic Ice Sheet. *Nature Geoscience*, *6*(11), 945–948.
903 https://doi.org/10.1038/ngeo1977

904 Lilien, D. A., Alley, K. E., & Alley, R. B. (2025). The effect of melt-channel geometry on ice-shelf flow. *Journal*
905 *of Glaciology*, *71*, e73. https://doi.org/10.1017/jog.2025.36

906 Markus, T., Neumann, T., Martino, A., Abdalati, W., Brunt, K., Csatho, B., Farrell, S., Fricker, H., Gardner, A.,
907 Harding, D., Jasinski, M., Kwok, R., Magruder, L., Lubin, D., Luthcke, S., Morison, J., Nelson, R.,
908 Neuenschwander, A., Palm, S., … Zwally, J. (2017). The Ice, Cloud, and land Elevation Satellite-2
909 (ICESat-2): Science requirements, concept, and implementation. *Remote Sensing of Environment*, *190*,
910 260–273. https://doi.org/10.1016/j.rse.2016.12.029

https://doi.org/10.5194/egusphere-2026-6522
Preprint. Discussion started: 19 November 2026
© Author(s) 2026. CC BY 4.0 License.

Marsh, O. J., & Rack, W. (2012). A method of calculating ice-shelf surface velocity using ICESat altimetry. *Polar Record*, *48*(1), 25–30. https://doi.org/10.1017/S0032247411000362

McGrath, D., Steffen, K., Holland, P. R., Scambos, T., Rajaram, H., Abdalati, W., & Rignot, E. (2014). The structure and effect of suture zones in the Larsen C Ice Shelf, Antarctica. *Journal of Geophysical Research: Earth Surface*, *119*(3), 588–602. https://doi.org/10.1002/2013JF002935

McGrath, D., Steffen, K., Rajaram, H., Scambos, T., Abdalati, W., & Rignot, E. (2012). Basal crevasses on the Larsen C Ice Shelf, Antarctica: Implications for meltwater ponding and hydrofracture. *Geophysical Research Letters*, *39*(16). https://doi.org/10.1029/2012GL052413

Mouginot, J., Scheuchl, B., & Rignot, E. (2017). MEaSUREs Antarctic Boundaries for IPY 2007-2009 from Satellite Radar, Version 2. *NASA National Snow and Ice Data Center Distributed Active Archive Center (DAAC) Data Set*, AXE4121732AD. https://doi.org/10.5067/AXE4121732AD

Neumann, T., Brenner, A., Hancock, D., Robins, J., Saba, J., Harbeck, K., Gibbons, A., Lee, J., Luthcke, S., & Rebold, T. (2023). *Ice, Cloud, and Land Elevation Satellite (ICESat-2) Project Algorithm Theoretical Basis Document (ATBD) for Global Geolocated Photons ATL03, version 6*. https://doi.org/10.5067/GA5KCLJT7LOT

Pang, A., Liang, Q., Li, W., Zheng, L., Li, T., & Cheng, X. (2023). The distribution and evolution of surface fractures on pan-Antarctic ice shelves. *International Journal of Digital Earth*, *16*(1), 3295–3320. https://doi.org/10.1080/17538947.2023.2246436

Qi, M., Liu, Y., Liu, J., Cheng, X., Lin, Y., Feng, Q., Shen, Q., & Yu, Z. (2021). A 15-year circum-Antarctic iceberg calving dataset derived from continuous satellite observations. *Earth System Science Data*, *13*(9), 4583–4601. https://doi.org/10.5194/essd-13-4583-2021

Rignot, E., Jacobs, S., Mouginot, J., & Scheuchl, B. (2013). Ice-Shelf Melting Around Antarctica. *Science*, *341*(6143), 266–270. https://doi.org/10.1126/science.1235798

Smith, B., Adusumilli, S., Csatho, B., Felikson, D., Fricker, H., Gardner, A., Holschuh, N., Lee, J., Nilsson, J., Paolo, F., Siegfried, M., Sutterley, T., & the ICESat-2 Science Team. (2025). *ATLAS/ICESat-2 L3A Land Ice Height, Version 7* [Data set]. NASA National Snow and Ice Data Center Distributed Active Archive Center. https://doi.org/10.5067/ATLAS/ATL06.007

Torres, R., Snoeij, P., Geudtner, D., Bibby, D., Davidson, M., Attema, E., Potin, P., Rommen, B., Floury, N., Brown, M., Traver, I. N., Deghaye, P., Duesmann, B., Rosich, B., Miranda, N., Bruno, C., L'Abbate, M., Croci, R., Pietropaolo, A., … Rostan, F. (2012). GMES Sentinel-1 mission. *Remote Sensing of Environment, The Sentinel Missions - New Opportunities for Science*, *120*, 9–24. https://doi.org/10.1016/j.rse.2011.05.028

Walker, C. C., & Gardner, A. S. (2019). Evolution of ice shelf rifts: Implications for formation mechanics and morphological controls. *Earth and Planetary Science Letters*, *526*, 115764. https://doi.org/10.1016/j.epsl.2019.115764

Wang, S., Alexander, P. M., Alley, R. B., Huang, Z., Parizek, B. R., Willet, A. G., & Anandakrishnan, S. (2025). Recent Variability in Fracture Characteristics and Ice Flow of Thwaites Ice Shelf, West Antarctica.

https://doi.org/10.5194/egusphere-2026-6522
Preprint. Discussion started: 19 November 2026
© Author(s) 2026. CC BY 4.0 License.



Journal of Geophysical Research: Earth Surface, *130*(5), e2024JF008118. https://doi.org/10.1029/2024JF008118

Wang, S., Alexander, P., Wu, Q., Tedesco, M., & Shu, S. (2021). Characterization of ice shelf fracture features using ICESat-2 – A case study over the Amery Ice Shelf. *Remote Sensing of Environment*, *255*, 112266. https://doi.org/10.1016/j.rse.2020.112266

Wesche, C., Jansen, D., & Dierking, W. (2013). Calving Fronts of Antarctica: Mapping and Classification. *Remote Sensing*, *5*(12), 6305–6322. https://doi.org/10.3390/rs5126305

Whiteford, A., Horgan, H. J., Leong, W. J., & Forbes, M. (2022). Melting and Refreezing in an Ice Shelf Basal Channel at the Grounding Line of the Kamb Ice Stream, West Antarctica. *Journal of Geophysical Research: Earth Surface*, *127*(11), e2021JF006532. https://doi.org/10.1029/2021JF006532